Formation, stability, and adiabatic excitation of peakons and double-hump solitons in parity-time-symmetric Dirac-$\delta(x)$-Scarf-II optical potentials

Ming Zhong,[1] Yong Chen,[2] Zhenya Yan,[3,4,*] and Shou-Fu Tian[1]

[1]*School of Mathematics, China University of Mining and Technology, Xuzhou 221116, China*

[2]*School of Mathematics and Statistics, Jiangsu Normal University, Xuzhou 221116, China*

[3]*Key Lab of Mathematics Mechanization, Academy of Mathematics and Systems Science, Chinese Academy of Sciences, Beijing 100190, China*

[4]*School of Mathematical Sciences, University of Chinese Academy of Sciences, Beijing 100049, China*

(Received 11 September 2021; accepted 17 December 2021; published 6 January 2022)

We introduce a class of physically intriguing $\mathcal{PT}$-symmetric Dirac-δ-Scarf-II optical potentials. We find the parameter region making the corresponding non-Hermitian Hamiltonian admit the fully real spectra, and present the stable parameter domains for these obtained peakons, smooth solitons, and double-hump solitons in the self-focusing nonlinear Kerr media with $\mathcal{PT}$-symmetric δ-Scarf-II potentials. In particular, the stable wave propagations are exhibited for the peakon solutions and double-hump solitons from some given parameters even if the corresponding parameters belong to the linear $\mathcal{PT}$-phase broken region. Moreover, we also find the stable wave propagations of exact and numerical peakons and double-hump solitons in the interplay between the power-law nonlinearity and $\mathcal{PT}$-symmetric potentials. Finally, we examine the interactions of the nonlinear modes with exotic waves, and the stable adiabatic excitations of peakons and double-hump solitons in the $\mathcal{PT}$-symmetric Kerr nonlinear media. These results provide the theoretical basis for the design of related physical experiments and applications in $\mathcal{PT}$-symmetric nonlinear optics, Bose-Einstein condensates, and other relevant physical fields.

DOI: 10.1103/PhysRevE.105.014204

I. INTRODUCTION

In general, the Hermiticity for Hamiltonians is required to admit the fully real spectra such that the corresponding modes can be observed in the traditional quantum mechanics [1]. However, Bender and Boettcher [2] introduced the concept of $\mathcal{PT}$ symmetry and found that a family of complex non-Hermitian $\mathcal{PT}$-symmetric Hamiltonians, $\mathcal{H} = -\partial_x^2 - (ix)^\sigma$ with $\sigma \geqslant 2$, could also possess the fully real spectra. A non-Hermitian Hamiltonian $\mathcal{H}$ is $\mathcal{PT}$ symmetric if $[\mathcal{H}, \mathcal{PT}] = 0$, where the parity operator $\mathcal{P}$ and time reversal $\mathcal{T}$ are defined as $\mathcal{P}$: $x \to -x$ and $\mathcal{T}$: $i \to -i$, respectively. Therefore, the $\mathcal{PT}$-symmetric condition of the complex linear Schrödinger operator $\mathcal{H}_{\mathcal{PT}} = -\partial_x^2 + U(x)$ is $U(x) = \mathcal{PT}U(x) = U^*(-x)$, which make the non-Hermitian Hamiltonians possibly admit the fully real spectra [3–8]. Moreover, the $\mathcal{PT}$-symmetric Hamiltonians have been experimentally verified in some fields such as optics, electronic circuits, mechanical systems, and microcavities [9–14]. Up to now, many types of $\mathcal{PT}$-symmetric potentials have been studied to support stable soliton propagations in the nonlinear physical models, such as the nonlinear Schrödinger (NLS) equation [15–31], derivative NLS equation [32], third-order NLS equation [33], and mass-modulated NLS equation [34]. The known $\mathcal{PT}$-symmetric potentials contain the Scarf-II potential [15,25,28,31], harmonic potential [24,25,29,35,36], Gaussian potential [23,37–39], super-Gaussian potential [40,41], Rosen-Morse potential [42,43], optical lattice potential [21,27,44,45], and others [46–48]. Therefore, the study of the different $\mathcal{PT}$-symmetric potentials can explore the generation mechanism of $\mathcal{PT}$-symmetric solitons (see, e.g., Refs. [49–55] and references therein).

Most of the above-mentioned linear and nonlinear modes are smooth functions. In fact, some nonsmooth functions were used to describe the linear and nonlinear modes in quantum mechanics and nonlinear optics [1,56,57]. For example, the Dirac $\delta(\mathbf{r})$ function can make the linear and nonlinear systems to generate the nonsmooth peakon modes [1]. Up to now, there exist a few works about the nonlinear wave equations with $\mathcal{PT}$-symmetric δ-function potentials [58–63]. A natural issue is whether other types of $\mathcal{PT}$-symmetric potentials can support other new types of stable nonsmooth peakons in the Kerr or even higher-order nonlinear media.

Motivated by these results and questions, in this paper, we would like to introduce a class of $\mathcal{PT}$-symmetric Dirac-δ-Scarf-II potential (2) containing the Scarf-II and δ-function potentials in the both Kerr and power-law nonlinear media to study the dynamical properties of the modified peakons and double-hump solitons with one sharp valley. Notice that the modified peakons $\mathrm{sech}(x)e^{\alpha|x|}$ ($\alpha < 0$) differ from the usual peakons $e^{-\omega|x|}$ ($\omega > 0$), and decay more quickly. These results will be useful to deeply understand the physical mechanism and properties of novel solitons in nonlinear media.

The main contributions of this paper can be summarized as follows:

(a) We introduce a class of $\mathcal{PT}$-symmetric Dirac-δ-Scarf-II potentia (2), which contains the Scarf-II potential. and $\mathcal{PT}$-symmetric δ-sgn-sech potential (4). Moreover, we give the parameter regions making the corresponding non-Hermitian Hamiltonians admit the fully real spectra (see Sec. III).

*Corresponding author: zyyan@mmrc.iss.ac.cn

(b) We find the exact solitons (9) of the cubic NLS equation (1) with the $\mathcal{PT}$-symmetric δ-sgn-sech potential (2) for the constraint $V_0 = 2\alpha$. Particularly, as $\alpha = 0$, we have the smooth solitons, but for $\alpha \neq 0$, we get the peakons with the amplitude $\frac{W_0}{3}\text{sech}x\, e^{\alpha|x|}$ and a nontrivial phase. In addition, we have the peakon solutions for $\alpha < 0$ and double-hump solitons for $0 < \alpha < 1$. These results differ from the usual peakons $e^{-\omega|x|}$ ($\omega > 0$).

(c) The above-mentioned exact solitons hold for the special propagation constants $\mu = 1 + \alpha^2$ (see Sec. IV A), but for the other cases of μ, we find the numerical peakons and double-hump solitons for the $\mathcal{PT}$-symmetric δ-Scarf-II potential (2) and $\mu \in [0, 10]$ (see Fig. 9 in Sec. IV C) and compare the numerical solutions with the exact solutions (see Fig. 8). We also study the numerical peakons and double-hump solitons of the cubic NLS equation with another type of the $\mathcal{PT}$-symmetric δ-sgn-sech potential (4) (see Fig. 10 in Sec. IV C).

(d) We explore the dynamical behaviors of high-order solitons of the NLS equation (1) with the $\mathcal{PT}$-symmetric potential (2) or (4) (see Sec. IV D).

(e) The interactions of peakons and solitons are studied. Furthermore, we study the stable adiabatic excitations of peakons and double-hump solitons (see Secs. V and VI).

(f) Finally, we also study the solitons of the generalized NLS equation with the power-law nonlinearity and $\mathcal{PT}$-symmetric potential (see Sec. IV E).

The rest of this paper is organized as follows. In Sec. II, we first introduce the nonlinear physical model with the $\mathcal{PT}$-symmetric Dirac-δ-Scarf-II potential and analyze the properties of the potential. In Sec. III, we investigate the curves for the $\mathcal{PT}$ unbroken and broken phases in the given parameter region. In Sec. IV, we find that the Kerr nonlinear media with the $\mathcal{PT}$-symmetric δ-Scarf-II potential can support the peakons and double-hump solitons. Moreover, we find their stable region and study the stable dynamical behaviors by numerical simulations. In order to further study the soliton anti-interference capability, in Sec. V we consider the interactions of two different types of solitons under the initial superposition of exotic isolated waves. In addition, we explore the dynamical behaviors of the two types of solitons in the excited states by means of adiabatic excitation in Sec. VI. Finally, we summarize some conclusions and discussions in Sec. VII.

II. KERR NONLINEAR PHYSICAL MODEL WITH THE $\mathcal{PT}$-SYMMETRIC POTENTIAL

A optical beam propagating in a self-focusing Kerr nonlinear medium with the refractive index $V(x)$ and gain-and-loss distribution $W(x)$ can be described by the NLS model with the complex potential in the dimensionless form [15,25]

$$i\partial_z\psi + \partial_x^2\psi - [V(x) + iW(x)]\psi + \delta n(I)\psi = 0, \quad (1)$$

where $\psi = \psi(x, z)$ denotes the envelope optical pulse, and x and z represent the transverse coordinates and propagation distance along the light beam, respectively. The nonlinear index $\delta n(I)$ is taken as the light intensity $I = |\psi|^2$, i.e., $\delta n(I) = |\psi|^2$. The $\mathcal{PT}$-symmetric external potential $V(x) + iW(x)$ requires that $V(x)$ and $W(x)$ are the even and odd functions, respectively. Equation (1) can also be associated with a variational principle $\delta\mathcal{L}(\psi, \psi^*)/\delta\psi^* = 0$ with the Lagrangian $\mathcal{L}(\psi, \psi^*) = \int_{\mathbb{R}}\{-\text{Im}(\psi\psi_z^*) + |\psi_x|^2 + [V(x) + iW(x)]|\psi|^2 - 1/2|\psi|^4\}dx$. Moreover, it is found that $\int_{\mathbb{R}}[\text{Im}(\psi\psi_z^*) - |\psi_x|^2 + |\psi|^4]dx = \int_{\mathbb{R}} V(x)|\psi|^2dx$. The power (alias mass or norm) and quasipower of Eq. (1) are defined as $N(z) = \int_{\mathbb{R}} |\psi(x, z)|^2dx$ and $Q(z) = \int_{\mathbb{R}} \psi\mathcal{PT}\psi dx$. The momentum $P(z) = \frac{i}{2}\int_{\mathbb{R}}(\psi\psi_x^* - \psi^*\psi_x)dx$. It is easy to prove that [15] $N_z = 2\int_{\mathbb{R}} W|\psi|^2dx$ and $Q_z = i\int_{\mathbb{R}} \psi(\mathcal{PT}\psi)[|\psi|^2 - |\psi(-x, z)|^2]dx$. In particular, $N_z = Q_z = 0$, that is, the power $N(z)$ and quasipower $Q(z)$ are conservative if $W(x)$ is an odd function and $\psi = \mathcal{PT}\psi$.

As we know, the Scarf-II and δ-function potentials can support the smooth solitons and nonsmooth peakons in the Kerr nonlinear media, respectively. In what follows, we would like to introduce a class of the physically interesting $\mathcal{PT}$-symmetric Dirac-δ-Scarf-II potential,

$$\begin{aligned} V(x) &= V_0[\delta(x) - \tanh|x|] - 2\,\text{sech}^2x, \\ W(x) &= -W_0\partial_x(\text{sech}x\, e^{\alpha|x|}), \end{aligned} \quad (2)$$

where $\alpha < 1$ and V_0, $W_0 \in \mathbb{R}$, to show that it can support the novel solitons in the Kerr nonlinear media. The complex $\mathcal{PT}$-symmetric potential (2) differs from the known Scarf-II and δ-function potentials, and has the following special cases for the different parameters V_0, α:

(i) As $V_0 = \alpha = 0$, the $\mathcal{PT}$-symmetric potential (2) reduces to the celebrated Scarf-II potential [3],

$$V(x) = -2\,\text{sech}^2x, \quad W(x) = W_0\text{sech}x\tanh x, \quad (3)$$

which are both smooth functions [see Figs. 1(a3) and 1(b3)]. We need to mention that the sperate energy level and the corresponding bound state of the Scarf-II potential have been studied in [64,65] and the references therein. The interaction of supersymmetry with $\mathcal{PT}$ symmetry and the generalized Scarf-II potential were also presented in the above work.

(ii) As $V_0 > 0$, $\alpha \in (0, 1)$, the $\mathcal{PT}$-symmetric potential (2) becomes the one with the real part being the δ-function-like potential and the imaginary part being the two-hump function [see Figs. 1(a2) and 1(b2)].

(iii) As $V_0 < 0$, $\alpha < 0$, the $\mathcal{PT}$-symmetric potential (2) becomes the one with the real part being the anti-δ-function-like potential and the imaginary part being the one-hump function [see Figs. 1(a1) and 1(b1)].

Figure 1 implies that the parameter α would modulate the real $V(x)$ and imaginary $W(x)$ parts of the $\mathcal{PT}$-symmetric potential. W_0 can control the amplitude of the gain-and-loss distribution. Since $W(x) \to 0$ as $|x| \to \infty$, the gain-and-loss distribution will affect the $\mathcal{PT}$-symmetric system in the limit domain.

In fact, we can also consider a similar and simplified version of the $\mathcal{PT}$-symmetric δ-Scarf-II potential (2), i.e., the $\mathcal{PT}$-symmetric δ-sgn-sech potential

$$\widehat{V}(x) = V_1\delta(x), \quad \widehat{W}(x) = W_1\,\text{sgn}\,x\,\text{sech}x\, e^{\alpha|x|}, \quad (4)$$

where V_1, $W_1 \in \mathbb{R}$, $\alpha < 1$. Near $x = 0$, these two potentials, given by Eqs. (2) and (4), are almost equivalent for $V_1 = V_0$, $W_1 = W_0(1 - \alpha)$. For $\alpha < 1$ and $V_0 = 2\alpha$, the profile of the $\mathcal{PT}$-symmetric δ-sgn potential (4) is similar to the one in Fig. 1.

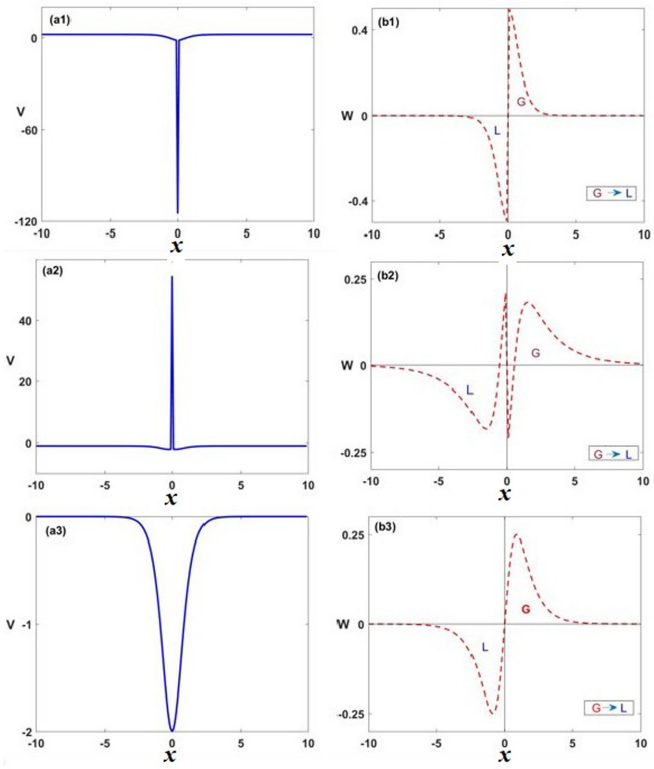

FIG. 1. Real and imaginary parts of the $\mathcal{PT}$-symmetric δ-Scarf-II potential: (a1),(b1) $(V_0,\ \alpha,\ W_0) = (-2, -1, 0.5)$; (a2),(b2) $(V_0,\ \alpha, W_0) = (1, 0.5, 0.5)$; (a3),(b3) $(V_0,\ \alpha, W_0) = (0, 0, 0.5)$.

III. $\mathcal{PT}$-PHASE BROKEN AND UNBROKEN CURVES OF THE LINEAR SPECTRAL PROBLEM

Here we consider the linear spectral problem with the given $\mathcal{PT}$-symmetric Dirac-δ-Scarf-II potential (2) and $\mathcal{PT}$-symmetric δ-sgn-sech potential (4),

$$\mathcal{H}_0\Phi(x) = \lambda\Phi(x), \quad \mathcal{H}_0 = \partial_x^2 - [V(x) + iW(x)], \tag{5}$$

where $\alpha < 1$, and the parameter region is chosen as $(V_j, W_j) \in [-2, 1] \times [0, 3]$ $(j = 0, 1.)$. Since the δ function cannot be used directly in the numerical calculations, we use the following parametric approximation of Gaussian function $\exp(-x^2/\epsilon^2)/(\epsilon\sqrt{\pi})$ $(\epsilon \to 0^+)$ to replace the $\delta(x)$. For the validity and accuracy of the results, here we take $\epsilon = 0.01$. And there exist some other parametric substitutions, such as $a/[\pi(x^2 + a^2)]$, $\sin(x/a)/(\pi x)$ for $a \to 0$. In fact, they are equivalent. We numerically solve the linear eigenvalue problem (5) by the spectral method [66–68] such that the $\mathcal{PT}$-symmetric broken and unbroken curves are found in the (V_j, W_j) space [see Figs. 2(a) and 2(b)] for choosing $\alpha = -1$, 0, 0.2, respectively. We need to point out that the $\mathcal{PT}$ phase is broken (unbroken) when the parameters are located above (below) the corresponding curve.

For the $\mathcal{PT}$-symmetric Dirac-Scarf-II potential given by Eq. (2), it can be seen that the $\mathcal{PT}$ unbroken area decreases as V_0 increases as $\alpha = -1$ and $\alpha = 0.2$. More intriguingly, if we choose $\alpha = 0$, the $\mathcal{PT}$ curves descend slowly when $V_0 \in (-2, -0.4)$, then increase for $V_0 \in (-0.4, -0.1)$, and, finally, decrease with a linear trend. And as mentioned in Ref. [3], as $V_0 = \alpha = 0$, Eq. (2) reduces to the Scarf-II potential, and the linear spectral problem (5) admits the entirely real spectra provided that $|W_0| \leqslant 9/4$, which checks the correctness of the $\mathcal{PT}$ broken curves deduced via the numerical method [see Figs. 2(a), 2(c2), 2(d2)]. For the given α and V_0, we examine the eigenvalues of the first lowest states [see Figs. 2(c1)–2(d3)]. We can make a conclusion that the spontaneous symmetry is broken due to the collision of the ground and the first several excited states. On account of the merge of the first energy levels, the imaginary parts would exist in the spectrum, which leads to the $\mathcal{PT}$-symmetry breaking.

As for the $\mathcal{PT}$-symmetric δ-sgn-sech potential (4), we also investigate the linear spectral problem (5). The $\mathcal{PT}$ broken and unbroken curves are displayed in Fig. 2(b). The unbroken phase cannot be found for $V_1 > 0$, which differs from the above potential (2). And the area of $\mathcal{PT}$ unbroken for $\alpha = -1$ is much wider than $\alpha = 0, 0.2$. As illustrated in [69], if we choose the potential $V(x) = \rho\delta(x)$, $W(X) \equiv 0$, then the linear problem given by Eq. (5) will not admit the real spectra for $\rho > 0$. This may be the main reason for the sharp conversion at $V_1 = 0$. And the corresponding energy levels indicate the $\mathcal{PT}$-phase break due to the collision of the first state, which is not shown here.

IV. THE STABILITY OF STATIONARY PEAKON AND DOUBLE-HUMP SOLITONS

A. The stationary solutions

In this section, we study the stability of the stationary solutions of Eq. (1). We find the localized stationary solitons of Eq. (1) with the $\mathcal{PT}$-symmetric δ-Scarf-II potential (2) in the form $\psi(x, z) = \phi(x)e^{i\mu z}$, where μ denotes the real-valued propagation constant and complex solution $\phi(x)$ satisfies

$$\frac{d^2\phi}{dx^2} - [V(x) + iW(x)]\phi + |\phi|^2\phi = \mu\phi, \tag{6}$$

whose real and imaginary parts generate

$$\mathrm{Re}\left(\frac{\phi_{xx}}{\phi}\right) + |\phi|^2 - V(x) = \mu, \quad \mathrm{Im}\left(\frac{\phi_{xx}}{\phi}\right) = W(x). \tag{7}$$

In general, it is difficult to seek the exact solutions of Eq. (6). One can usually solve Eq. (6) by the numerical methods such as the spectral renormalization method [70] or modified squared-operator iteration method [71]. However, it is interesting to find the exact solution of Eq. (6) in some special cases by the resolution methods [25,28]. We can take the complex function as $\phi(x) = \rho(x)\exp[i\int_0^x \varphi(s)ds]$, with $\rho(x)$ being a real-valued amplitude function and $\varphi(x)$ a real-valued function of the hydrodynamic velocity. As a result, we know that they solve the coupled nonlinear equations

$$\rho_{xx} = \left\{V(x) - \rho^2 + \rho^{-4}\left[\int_0^x W(s)\rho^2(s)ds\right]^2 + \mu\right\}\rho,$$
$$\varphi(x) = \rho^{-2}\int_0^x W(s)\rho^2(s)ds. \tag{8}$$

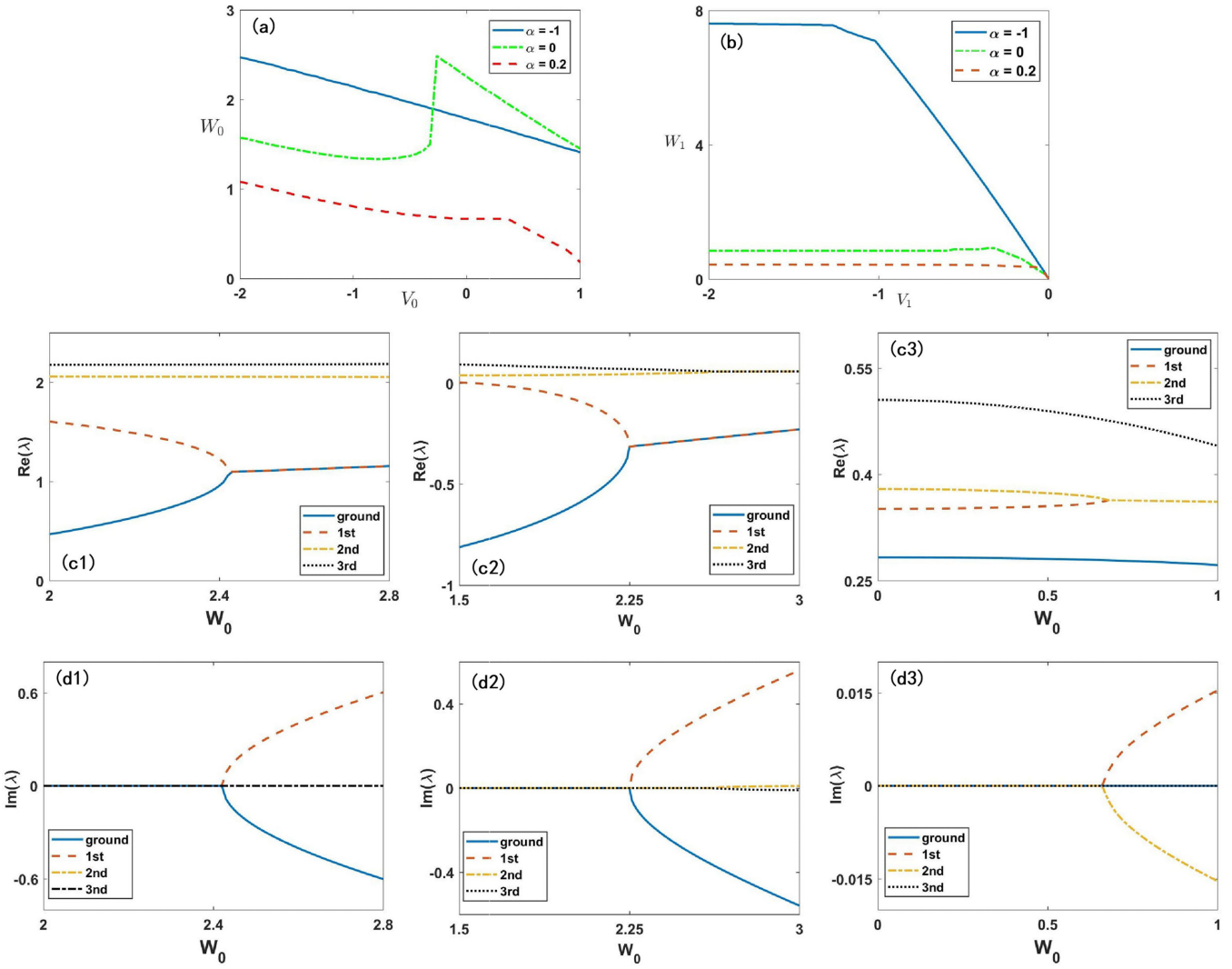

FIG. 2. (a),(b) $\mathcal{PT}$ unbroken and broken curves of Eq. (5) with the $\mathcal{PT}$-symmetric δ-Scarf-II potential (2) and δ-sgn-sech potential (4). Real and imaginary parts of the first four energy levels λ as a function of W_0 at (c1),(d1) $V_0 = -2,\ \alpha = -1$; (c2),(d2) $V_0 = \alpha = 0$; and (c3),(d3) $V_0 = 0.4,\ \alpha = 0.2$.

For the given $\mathcal{PT}$-symmetric δ-Scarf-II potential (2), from Eq. (8) we find that $\phi(x)$ is of the form

$$\phi(x) = \frac{W_0}{3}\mathrm{sech}x\, e^{\alpha|x|}\exp\left(-\frac{iW_0}{3}\int_0^x \mathrm{sech}s\, e^{\alpha|s|}ds\right), \tag{9}$$

with $\mu = 1+\alpha^2$ and $V_0 = 2\alpha$. Thus we have the density of the stationary solution $|\psi(x,z)| = \frac{W_0}{3}\mathrm{sech}x\, e^{\alpha|x|}$ $(\alpha < 1)$, where the gain-and-loss parameter W_0 can control the amplitude of the soliton, and another parameter α can modulate the profiles of the solitons:

(a) As $\alpha = 0$, the solution becomes the usual smooth bright soliton $|\psi(x,z)| = \frac{W_0}{3}\mathrm{sech}x$ and the corresponding potential degenerates to the Scarf-II potential, which have been analyzed [15].

(b) However, as $\alpha \neq 0$, we have the novel solitons. As $\alpha < 0$, we have the density of the modified peakon solution, $|\psi(x,z)| = \frac{W_0}{3}\mathrm{sech}x\, e^{\alpha|x|}$, which decays more quickly than the usual peakon $e^{\alpha|x|}$ as $|x|$ grows (see Fig. 4); that is, for the fixed $\alpha < 0$, the peakon solution (9) is of a smaller wave width than the known peakon. It is easy to know that the density $|\psi(x,z)|$ is a continuous function of x, but has no first-order derivatives at the peak point $x = 0$. It has the finite-order weak derivatives in the sense of distributions such as

$$\begin{aligned}\frac{d|\psi|}{dx} &= \frac{W_0}{3}\mathrm{sech}x\, e^{\alpha|x|}(\alpha\,\mathrm{sgn}(x) - \tanh x),\\ \frac{d^2|\psi|}{dx^2} &= \frac{W_0}{3}\mathrm{sech}x\, e^{\alpha|x|}(2\alpha\delta(x) - 2\alpha\tanh|x|\\ &\quad -2\,\mathrm{sech}^2 x + \alpha^2 + 1).\end{aligned} \tag{10}$$

(c) When $0 < \alpha < 1$, since the growing velocity of $e^{\alpha|x|}$ is smaller than the decaying velocity of $\mathrm{sech}x$ $(\mathrm{sech}x \leqslant 2e^{-|x|})$, we find the novel soliton (9) with double humps and one sharp valley (see Fig. 5), which is also a continuous function of x but has no first-order derivatives at the sharp valley point $x = 0$.

Since $\phi(x)$ given by Eq. (9) is $\mathcal{PT}$ symmetric, the quasipower Q and power P are equivalent. Moreover, they are both conservative since they are both the same limited

constant:

$$N = Q = \int_{\mathbb{R}} \frac{W_0^2}{9} \mathrm{sech}^2 s\, e^{2\alpha|s|} ds$$
$$\leqslant \int_{\mathbb{R}} \frac{2W_0^2}{9} e^{2(\alpha-1)|s|} ds = \frac{2W_0^2}{9(1-\alpha)}, \quad \alpha < 1, \quad (11)$$

where we have used the inequality $\mathrm{sech} x \leqslant 2e^{-|x|}$.

B. Spectral stability analysis of stationary solutions

In what follows, we study the spectral stability analysis of the obtained stationary peakons and double-hump solitons with one sharp valley, given by Eq. (9), of Eq. (1) by considering the perturbed solution,

$$\psi(x,z) = \{\phi(x) + \nu[F_1(x)e^{i\varepsilon z} + F_2(x)e^{-i\varepsilon^* z}]\}e^{i\mu z}, \quad (12)$$

where $\nu \ll 1$, $F(x)$ and $G(x)$ represent the corresponding eigenfunctions of the linearized problems, and ε indicates the growth rate of the instability. Then, substituting it into Eq. (1) and linearizing with respect to ν generate the following eigenvalue problem:

$$\begin{pmatrix} \mathcal{H}_0 + 2|\phi|^2 - \mu & \phi^2(x) \\ -\phi^{*2}(x) & -\mathcal{H}_0^* - 2|\phi|^2 + \mu \end{pmatrix} \begin{pmatrix} F_1 \\ F_2 \end{pmatrix} = \varepsilon \begin{pmatrix} F_1 \\ F_2 \end{pmatrix}, \quad (13)$$

where $\mathcal{H}_0$, $\phi(x)$ are given by Eqs. (5) and (9) and $\mu = \alpha^2 + 1$.

It is obvious that if $|\mathrm{Im}(\varepsilon)| > 0$, then one of the two terms $e^{i\varepsilon z}$ and $e^{-i\varepsilon^* z}$ approaches infinity as $z \to +\infty$ such that the solution will grow at an exponential rate as $z > 0$ grows, and is linear unstable; otherwise, the solution is linear stable. The above eigenvalue problem can be solved by the Fourier collocation method [68]. To conveniently describe the spectra of the above eigenvalue problem, we define the linear instability index (i.e., the color bar in Fig. 3) $\chi = \log(\max\{|\mathrm{Im}(\varepsilon)|\})$ of the stationary solution, where log represents the common logarithm. It follows from the errors of the numerical calculation and the simulation results of beam propagation shown below that we find that the stationary solution is linearly stable for the area of $\chi(\alpha, W_0) \leqslant -6$ in most cases; otherwise, it is unstable (see Fig. 3). Notice that one may consider the other areas, e.g., $\chi(\alpha, W_0) \leqslant -7$ for the linear stability. Due to the symmetry of W_0, we only consider $W_0 \geqslant 0$. We can conclude that the stable domain becomes narrower as α grows. Moreover, a sharp transition can be found at $\alpha = 0$, which coincides with the $\mathcal{PT}$ broken curve.

To further analyze the dynamical behaviors of the nonlinear modes (9), we resort to the beam propagation method with the initial condition $\psi(x, z = 0) = \phi(x)(1 + \epsilon)$, where $\phi(x)$ is a nonlinear mode given by Eq. (9), and $\epsilon = 0.02\,\mathrm{rand}(N, 1)\,(1 + i)$ is a complex broadband 2% random perturbation with $\mathrm{rand}(N, 1)$ which is an $N \times 1$ array of pseudorandom uniform values on the open interval $(0, 1)$. As mentioned above, we first consider the peakon solitons for $\alpha < 0$. Based on the above-mentioned critical $\mathcal{PT}$ broken curve, we first take $\alpha = -1$ and $W_0 = 1$, where the parameters are located in both the $\mathcal{PT}$ unbroken region [linear case; see Fig. 2(a)] and stable domain (nonlinear case; see Fig. 3). Figure 4(a1) indicates the stable peakon solution for a long propagation distance, where the initial condition is displayed

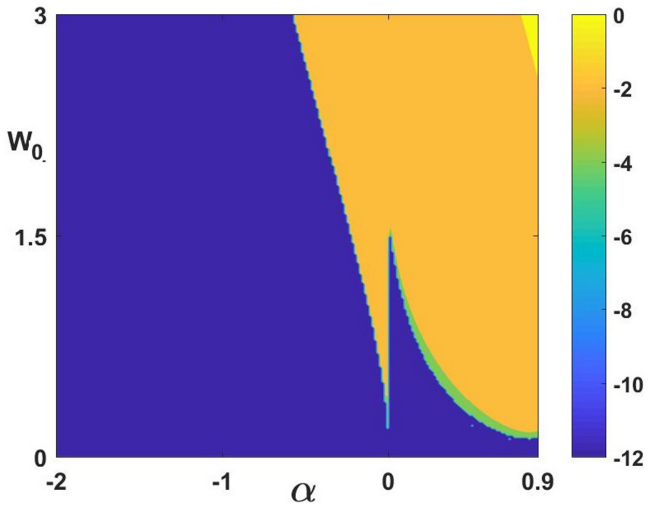

FIG. 3. Linear stable and unstable regions of the solution (9) in the $\mathcal{PT}$-symmetric δ-Scarf-II potential (2) by studying Eq. (13), where the blue region corresponds to the stable region, and the rest of the domain corresponds to the unstable region (the color bar is defined by the values $\log(\max\{|\mathrm{Im}(\varepsilon)|\})$, e.g., -8 denotes $\max\{|\mathrm{Im}(\varepsilon)| = 10^{-8}\}$. Notice that $\alpha < 0$, $\alpha = 0$, and $0 < \alpha < 1$ correspond to the peakon, smooth soliton, and double-hump soliton, respectively.

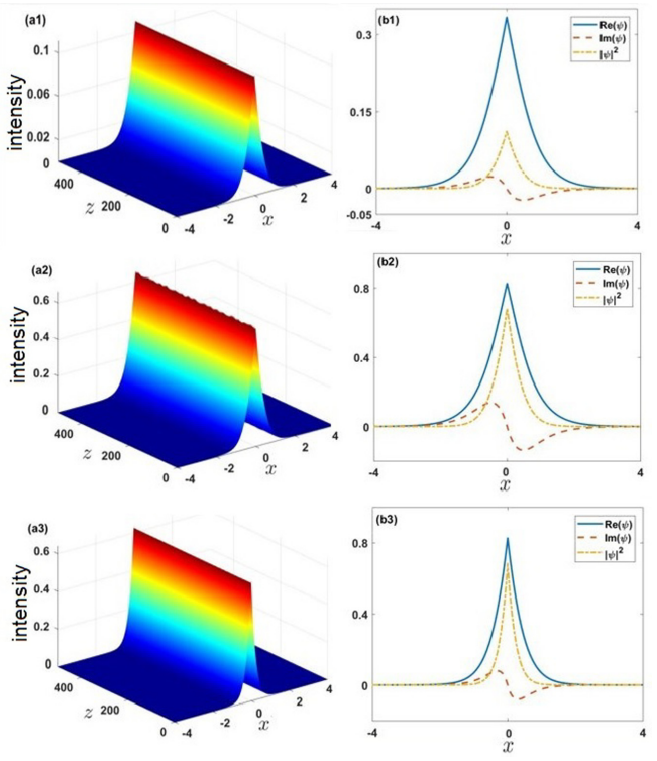

FIG. 4. The stable wave propagations of peakon solutions (9) with a 2% random white noise for $\alpha < 0$: (a1) $\alpha = -1$, $W_0 = 1$ ($\mathcal{PT}$ unbroken, linear stable); (a2) $\alpha = -1$, $W_0 = 2.48$ ($\mathcal{PT}$ broken, linear stable); (a3) $\alpha = -2$, $W_0 = 2.48$ ($\mathcal{PT}$ unbroken, linear stable). (b1)–(b3) The corresponding initial conditions of the peakon solutions (9).

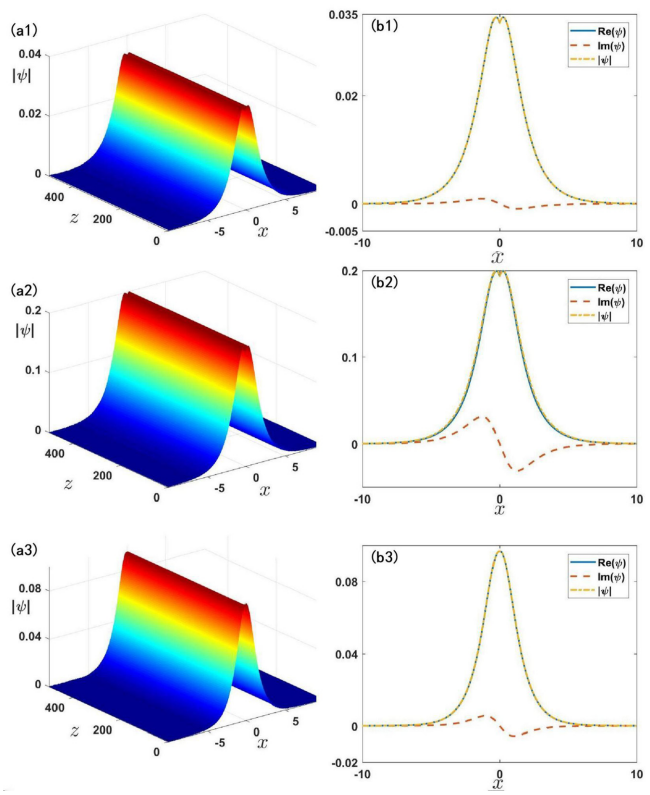

FIG. 5. The stable wave propagations of double-hump solitons with one sharp valley (9) with a 2% random white noise for $0 < \alpha < 1$: (a1) $\alpha = 0.25$, $W_0 = 0.1$ ($\mathcal{PT}$ unbroken, linear stable); (a2) $\alpha = 0.25$, $W_0 = 0.58$ ($\mathcal{PT}$ broken, linear stable); (a3) $\alpha = 0.04$, $W_0 = 0.29$ ($\mathcal{PT}$ unbroken, linear stable). (b1)–(b3) The corresponding initial condition of the soliton solutions (9).

in Fig. 4(b1). If we fix $\alpha = -1$, and change W_0 from 1 to 2.48, then the spectra become complex at the two lowest energy states. That is, the parameters $(\alpha, W_0) = (-1, 2.48)$ are located in the $\mathcal{PT}$ broken region [linear case; see Fig. 2(a)], but we still find the stable peakon solution [see Fig. 4(a2)]. However, as we fix $W_0 = 2.48$ and take $\alpha = -2$, the spectra are all real again. That is, the parameters $(\alpha, W_0) = (-2, 2.48)$ are located in the $\mathcal{PT}$ unbroken region [linear case; see Fig. 2(a)], and the parameters are also located in the linear stable area [see Fig. 4(a3)]. We can conclude that the stability of the solitons can be modulated by the nonlinear term and the $\mathcal{PT}$-symmetric parameters together from the above-mentioned numerical simulations.

However, for $\alpha > 0$, we find the double-hump solitons (9) with one sharp valley of Eq. (1), which have the strong stability. Since the transition occurs at $\alpha = 0$, the $\mathcal{PT}$ unbroken domain is narrower. We choose $\alpha = 0.25$ and $W_0 = 0.1$, which are located in the $\mathcal{PT}$ unbroken region [see Fig. 2(a)], such that the double-hump soliton is stable [see Fig. 5(a1)]. We then fix $\alpha = 0.25$ and change $W_0 = 0.58$, which are located in the $\mathcal{PT}$ broken region [see Fig. 2(a)]. However, we find that the double-hump soliton is still stable [see Fig. 5(a2)]. The main reason for this stable phenomenon is that the nonlinear term can modulate the linear $\mathcal{PT}$ spectra; that is, for some parameters, the nonlinear action can excite

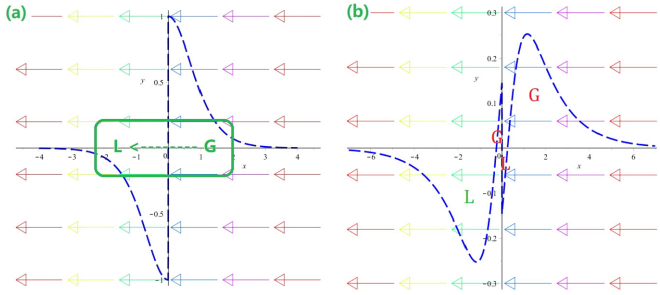

FIG. 6. The transverse power-flow or "Poynting vector" (14) related to nonlinear modes (9) and gain-and-loss distribution $W(x)$ given by Eq. (2) (dashed lines) with (a) $\alpha = -1$, $W_0 = 1$, and (b) $\alpha = 0.25$, $W_0 = -0.58$.

the $\mathcal{PT}$-symmetric broken phase to the $\mathcal{PT}$-symmetric unbroken phase. Finally, we take $\alpha = 0.04$, $W_0 = 0.29$, which are located in the $\mathcal{PT}$ unbroken region [see Fig. 2(a)], such that the double-hump soliton is found to be stable [see Fig. 5(a3)].

In conclusion, we have found the stable peakons and double-hump solitons of Eq. (1) for $\alpha < 0$ or $0 < \alpha < 1$. The obtained results indicate that the larger the strength W_0 of the gain-and-loss distribution, the more unfavorable the generation of stable solitons. We also investigate the potential energy for those parameters located in both the $\mathcal{PT}$ broken region and linearly unstable domain, which are not shown here. Apparently, the stability depends on the $\mathcal{PT}$ phase for modes in the linear spectral problem. However, the $\mathcal{PT}$-symmetric potential and nonlinear term both play the key roles in the nonlinear $\mathcal{PT}$-symmetric systems, which is typical in Kerr nonlinear media with $\mathcal{PT}$-symmetry potential (see, e.g., [15,24]). And this also holds for the instabilities in the dynamical simulations [72].

Apart from this, we also pay attention to the transverse power-flow intensity associated with the nonlinear solutions, which is defined by $S(x) = (i/2)(\phi\phi_x^* - \phi^*\phi_x) = |\phi|^2[\arg(\phi)]_x$, where $\arg(\phi)$ represents the phase function of $\phi(x)$. It follows from (9) that we have the transverse power-flow intensity $S(x)$ as

$$S(x) = -\frac{W_0^3}{27}\operatorname{sech}^3 x\, e^{3\alpha|x|}. \tag{14}$$

It is not hard to find that the sign of $S(x)$ depends on the gain-loss strength W_0. Equation (14) indicates that the power always flows from the gain toward the loss regions (see Fig. 6).

C. Numerical stationary solutions and stability

Case 1. $\mathcal{PT}$-symmetric Dirac-δ-Scarf-II potential (2). In the section above, we study the linear stability of exact stationary solutions (9) for $\mu = 1 + \alpha^2$ of Eq. (1) with the $\mathcal{PT}$-symmetric δ-Scarf-II potential (2). We now study its numerical solutions by considering Eq. (6) for the other propagation distance $\mu \neq 1 + \alpha^2$ by the spectral renormalization method [70]. First, we compare the exact solutions with numerical solutions for the different α (see Fig. 7) to illustrate the validity of the used numerical method. It is worth pointing out that we take $\phi(x) = \operatorname{sech} x$, $r = 1000$ as the initial state,

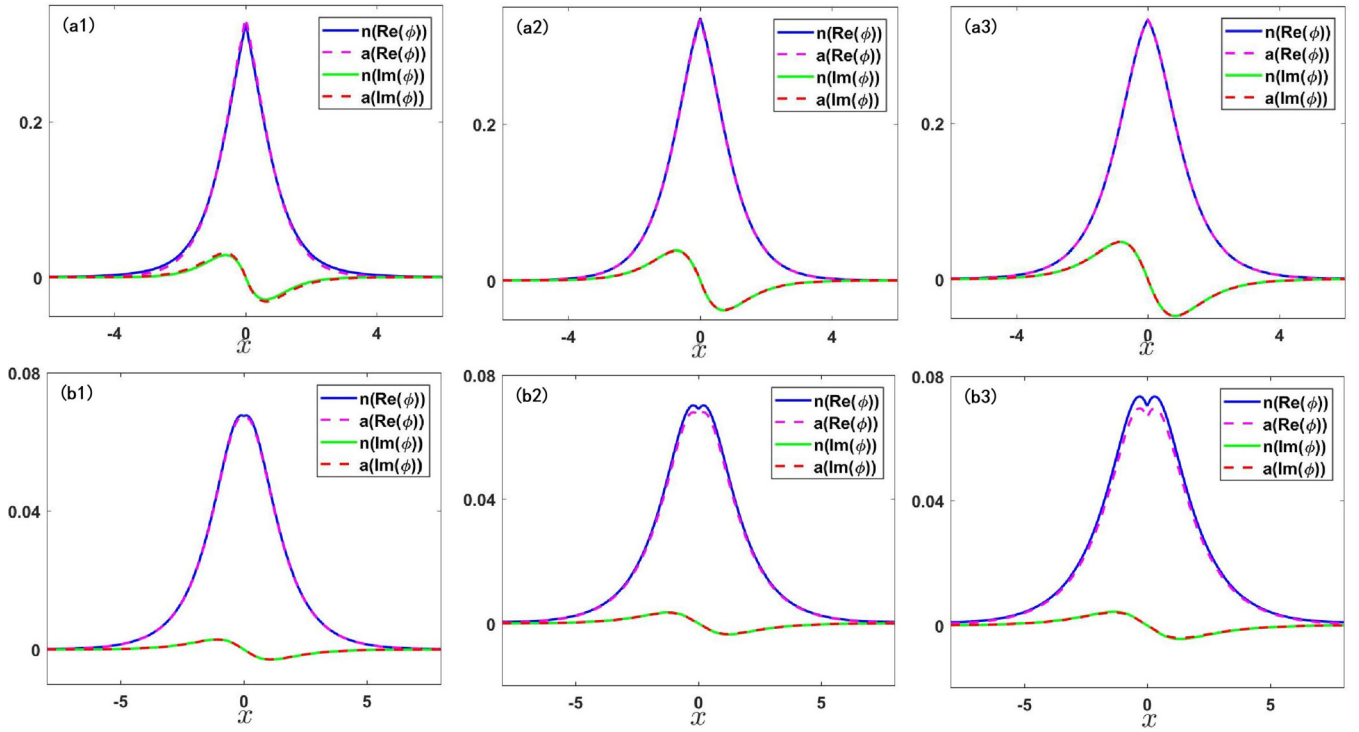

FIG. 7. Comparisons between exact and numerical solutions, where n(Re(ϕ)) [a(Re(ϕ))] and n(Im(ϕ)) [a(Im(ϕ))] represent the real part and imagine part of the numerical [exact] solutions, respectively. (a1) $\alpha = -0.6$, $W_0 = 1$; (a2) $\alpha = -0.4$, $W_0 = 1$; (a3) $\alpha = -0.2$, $W_0 = 1$; (b1) $\alpha = 0.1$, $W_0 = 0.2$; (b2) $\alpha = 0.2$, $W_0 = 0.2$; (b3) $\alpha = 0.3$, $W_0 = 0.2$.

and the maximum number of iterations is 4000. Without loss of generality, we choose $\mu \in [0, 10]$.

For the case $\alpha < 0$, we set $W_0 = -1$, and the power curves for the different $\alpha = -0.6$, -0.4, and -0.2 are displayed in Fig. 8(a), which first decrease, and then increase as μ grows. It follows from the numerical results that the μ decreases as the α increases so that the power reaches its minimum point. Meanwhile, the turning point is about $\mu = 1$, that is, $\alpha = 0$ [notice that the existence condition of the exact solutions (9) is $\mu = 1 + \alpha^2$], in which the $\mathcal{PT}$-symmetric potential (2) degenerates to the Scarf-II potential, and the corresponding solution (9) becomes the smooth soliton. This may be due to the effect of the smoothness of the solution on the soliton power. And the lowest cutoffs for the existing ranges of numerical solitons show a growth trend, i.e., $\mu = 0$, 0.1, 0.6 as α increases from -0.6 to -0.4, -0.2. Moreover, we utilize the beam propagation method to simulate the propagation behaviors of solitons for different parameters such that we found that the high-power solitons seem to have better propagation stability than the low-power solitons. We first choose $\alpha = -0.6$, $\mu = 1$ to generate the unstable wave propagation [see Figs. 8(a1) and 8(a2)]. Second, if we take $\alpha = -0.4$, $\mu = 3$ corresponding to the higher-power solution, then we find that the solution is stable [see Figs. 8(a3) and 8(a4)]. Finally, for $\alpha = -0.2$, $\mu = 5$, we can also find a stable higher-power soliton [see Figs. 8(a5) and 8(a6)].

For the case $\alpha > 0$, we choose $W_0 = 0.2$ and $\alpha = 0.1$, 0.2, 0.3 belonging to the $\mathcal{PT}$-phase unbroken region [see Fig. 2(a)]. The power curves are displayed in Fig. 8(b), which first decrease, and then increase as μ grows. We also obtain the corresponding numerical solitons and perform their wave propagations for different potential parameters. First, we set $\alpha = 0.1$, $\mu = 1$, and find that the numerical soliton is stable [see Figs. 8(b1) and 8(b2)]. And we take $\alpha = 0.2$, $\mu = 3$, and find that the soliton seems to possibly be stable propagation in a short distance ($z < 300$), but its instability occurs as the propagation distance becomes increasingly larger [see Figs. 8(b3) and 8(b4)]. Finally, we consider $\alpha = 0.3$, $\mu = 5$ corresponding to the higher-power soliton, and find that its instability appears quickly [see Figs. 8(b5) and 8(b6)]. Thus we may conclude that the low-power solitons are more stable in this condition, which differs from the case $\alpha < 0$.

Case 2. $\mathcal{PT}$-symmetric δ-sgn-sech potential (4). We also focus on the dynamic behaviors of solutions of Eq. (1) with the $\mathcal{PT}$-symmetric δ-sgn-sech potential (4). We investigate the ground-state solution of Eq. (6) with the potential (4) using the above-mentioned numerical method. By the numerical experiments, we are surprised to find from Eq. (6) that the $\mathcal{PT}$-symmetric δ-sgn-sech potential (4) supports the peakon solution for $\alpha < 0$, while for the case $\alpha > 0$, we find its double-hump solutions, which have the same profiles as those in the $\mathcal{PT}$-symmetric δ-Scarf-II potential (2). We consider the propagation constant $\mu \in (0, 5)$ whether $\alpha > 0$ or $\alpha < 0$. For $\alpha < 0$, we fix $W_1 = -1$, $\alpha = -1$, and we have the power curve in Fig. 9(a1), and the corresponding linear stability in Fig. 9(a2). The small μ for the existence of numerical solitons is 1.2. We choose two different parameters located in linear stable and unstable regions to investigate the wave propagations, respectively. First, for the considered $\mu = 1.5$, the numerical soliton and wave propagation are displayed

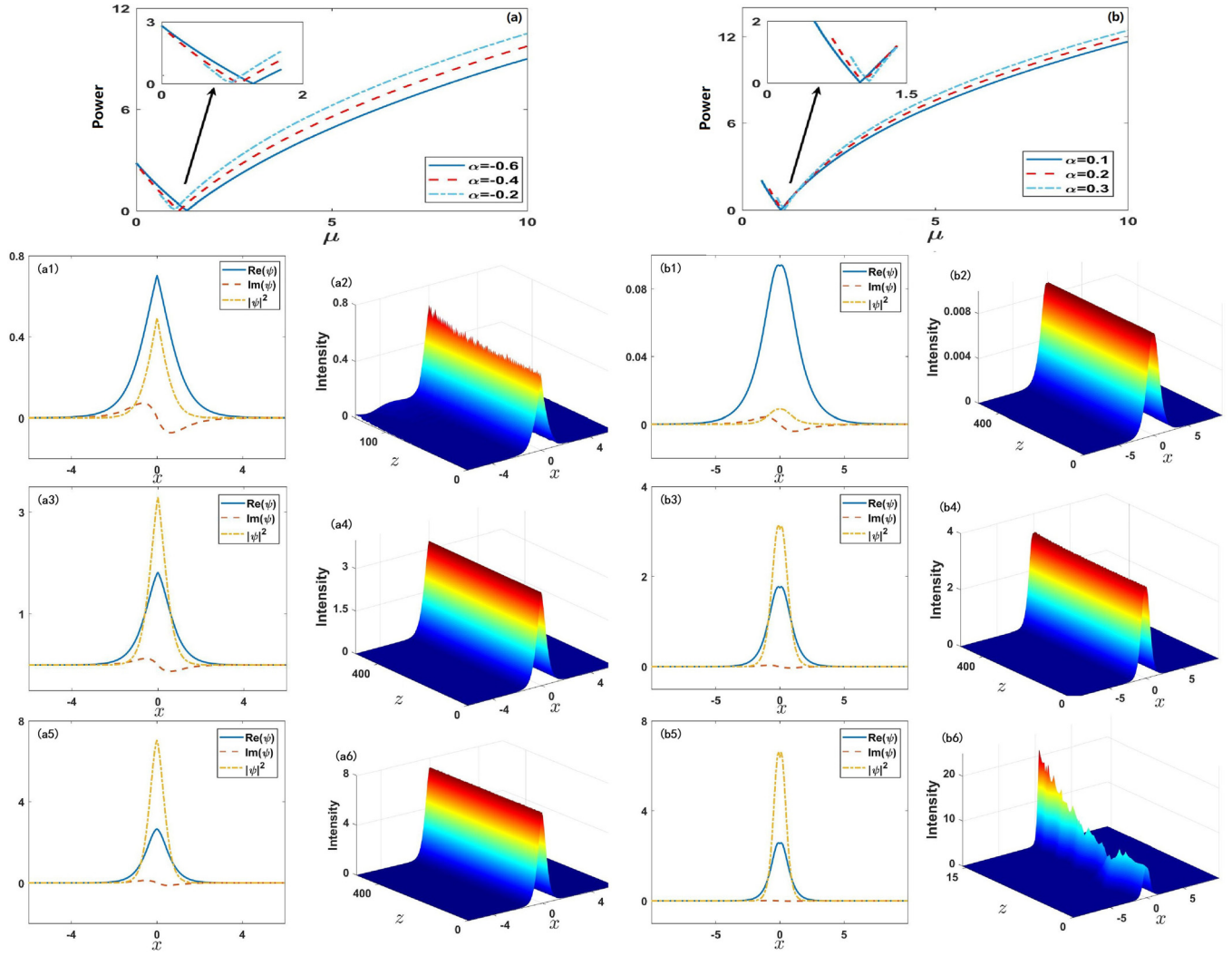

FIG. 8. The power vs the propagation constant μ for the potential (2) at (a) $W_0 = 1$, $\alpha < 0$ and (b) $W_0 = 0.2$, $0 < \alpha < 1$. Numerical solitons and their wave propagations: (a1),(a2) $\alpha = -0.6$, $\mu = 1$ (unstable); (a3),(a4) $\alpha = -0.4$, $\mu = 3$ (stable); (a5),(a6) $\alpha = -0.2$, $\mu = 5$ (stable); (b1),(b2) $\alpha = 0.1$, $\mu = 1$ (stable); (b3),(b4) $\alpha = 0.2$, $\mu = 3$ (semistable); (b5),(b6) $\alpha = 0.3$, $\mu = 5$ (unstable).

in Figs. 9(a3) and 9(a4), which indicates a stable periodic phenomenon. Then we choose $\mu = 4$, interestingly enough, such that we also have a stable soliton in the linear unstable region [see Figs. 9(a5) and 9(a6)], whose main reason is that the corresponding phase is $\mathcal{PT}$ unbroken. In what follows, we investigate $\alpha > 0$. We choose $\alpha = 0.5$, $W_0 = 0.4$. The power curve [see Fig. 9(b1)] is monotonically increasing as μ grows, which has a different trend compared to the above cases. By solving the linear stability problem (13), all numerical solitons are shown to be linear unstable [see Fig. 9(b2)], whose main reason is that the corresponding phase is $\mathcal{PT}$ broken [see Fig. 2(b)]. For $\mu = 2$, 4, we utilize the spectral renormalization method [70] to deduce the profile [see Figs. 9(b3) and 9(b4)]. Then we use the beam propagation method to get the unstable dynamical behavior in Figs. 9(b5) and 9(b6).

D. High-order solitons and wave propagations

In this section, we would like to consider the high-order solitons of the NLS equation (1) with the $\mathcal{PT}$-symmetric potential (2) or (4). Inspired by Ref. [31], we take the following initial state:

$$\phi(x) = a|x|^b e^{-x^2/c^2}, \tag{15}$$

where a, c represent the height and the width of the wave, respectively, and the parameter b is used to modulate the number of peaks. First, we investigate the existence and stability of high-order solitons of Eq. (1) with the potential (2). The profile and the evolution of two-hump soliton are displayed in Figs. 10(a1) and 10(a2), which denote an unstable propagation. And by changing the parameters, we obtain a three-hump soliton and its unstable dynamical behavior [see Figs. 10(b1) and 10(b2)]. In what follows, we study the high-order solitons of Eq. (1) with the $\mathcal{PT}$-symmetric δ-sgn-sech potential (4). By appropriating parameters, we obtain the two-hump solution as well as the unstable evolution [see Figs. 10(c1) and 10(c2)]. Finally, we numerically get the three-hump soliton, unlike the previous case, and the semistable propagation state is illustrated in Figs. 10(d1) and 10(d2). The middle peak remains unchanged during propagation, while the two peaks next to it propagate away with a bend trend.

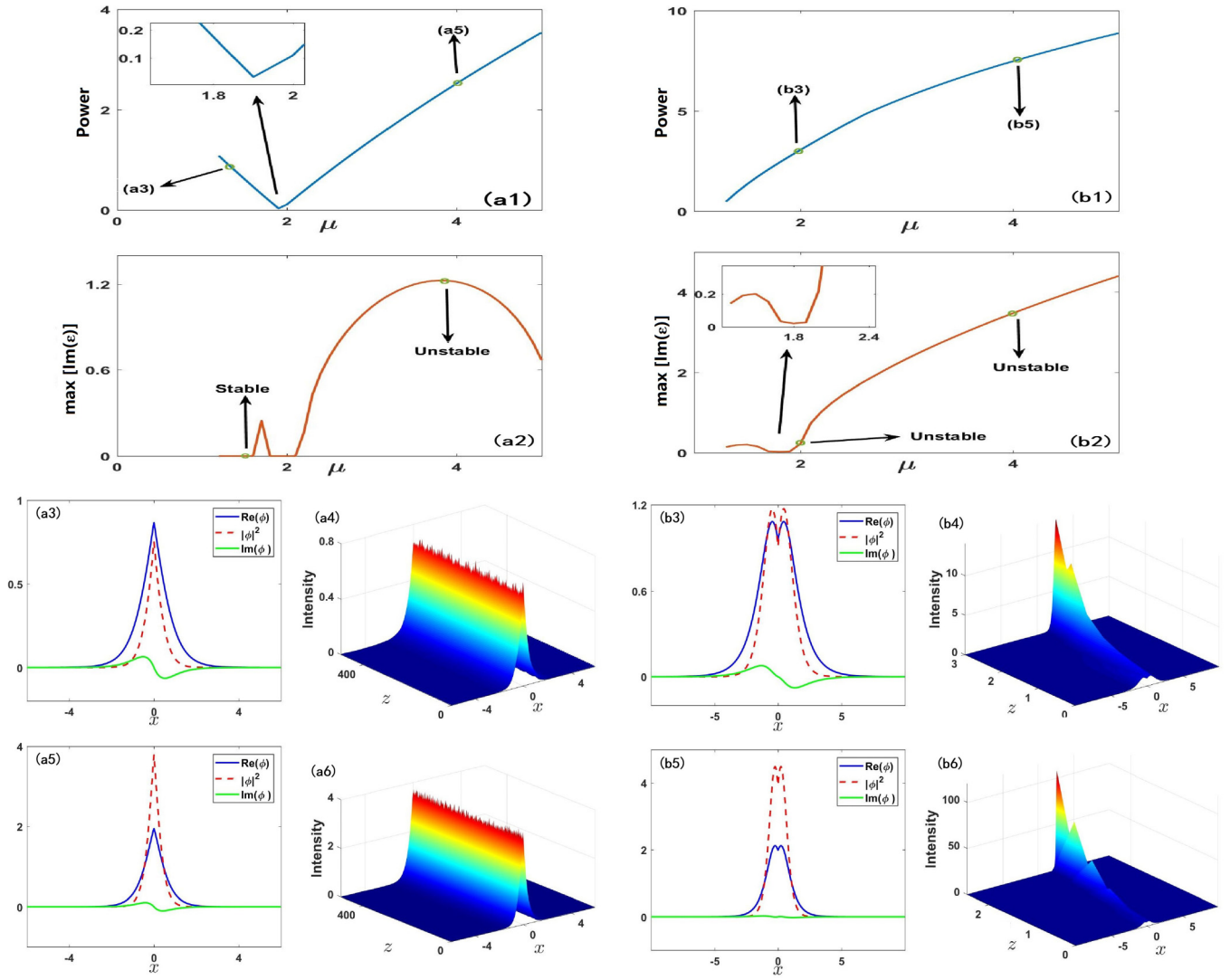

FIG. 9. The power vs the propagation constant μ for the potential (4) at (a1) $W_1 = 1$, $\alpha = -1$ and (b1) $W_0 = 0.4$, $\alpha = 0.5$. The curves of $\log(\max\{|\mathrm{Im}(\varepsilon)|\})$ corresponding to the linear stability [cf. Eq. (13)] with the marked "stable" and "unstable" points at (a2) $W_1 = 1$, $\alpha = -1$ and (b2) $W_0 = 0.4$, $\alpha = 0.5$. Numerical solitons and their wave propagations: (a3),(a4) $\mu = 1.5$ (stable); (a5),(a6) $\mu = 4$ (stable); (b3),(b4) $\mu = 2$ (unstable); (b5),(b6) $\mu = 4$ (unstable).

E. The generalized NLS equation with power-law nonlinearity and $\mathcal{PT}$-symmetric potential

Similarly, we now turn to the case of a power-law medium with $\delta n(I)$ taken as the form $\delta n(I) = |\psi|^{2\sigma}$ ($\sigma > 0$) such that Eq. (1) is changed into the NLS equation with power-law nonlinearity and $\mathcal{PT}$-symmetric potential,

$$i\partial_z\psi + \partial_x^2\psi - [V(x) + iW(x)]\psi + |\psi|^{2\sigma}\psi = 0, \quad \sigma > 0. \tag{16}$$

Equation (16) can also be associated with a variational principle $\delta\mathcal{L}(\psi, \psi^*)/\delta\psi^* = 0$ with the Lagrangian $\mathcal{L}(\psi, \psi^*) = \int_{\mathbb{R}}\{-\mathrm{Im}(\psi\psi_z^*) + |\psi_x|^2 + [V(x) + iW(x)]|\psi|^2 - 1/(\sigma+1)|\psi|^{2(\sigma+1)}\}dx$.

For the given $\mathcal{PT}$-symmetric Dirac-δ-Scarf-II potential

$$V(x) = 2\alpha\beta[\delta(x) - \beta\tanh|x|] - (\beta^2 + \beta)\mathrm{sech}^2 x,$$
$$W(x) = -W_0\partial_x(\mathrm{sech}x\, e^{\alpha|x|}), \tag{17}$$

with $\alpha < 1$, $\beta = 1/\sigma$, $W_0 \in \mathbb{R}$, we can find that Eq. (16) admits the peakon solution ($\alpha < 0$), double-hump soliton ($0 < \alpha < 1$), and smooth soliton ($\alpha = 0$) in the form

$$\psi(x, z) = \pm\left(\frac{|W_0|}{2\beta + 1}\mathrm{sech}x\, e^{\alpha|x|}\right)^{\beta} e^{i\mu z} \times \exp\left(-\frac{iW_0}{2\beta + 1}\int_0^x \mathrm{sechs}\, e^{\alpha|s|}ds\right), \tag{18}$$

with $\mu = \beta^2(1 + \alpha^2)$. In particular, at $\sigma = \beta = 1$, the potential (17) and solutions (18) reduce to the above-mentioned results given by Eqs. (9) and (2), respectively.

In what follows, we mainly consider Eq. (16) with $\sigma = 1/2$ and $\sigma = 2$, which corresponds to the quadratic NLS equation

$$i\partial_z\psi + \partial_x^2\psi - [V(x) + iW(x)]\psi + |\psi|\psi = 0 \tag{19}$$

and critical quintic NLS equation

$$i\partial_z\psi + \partial_x^2\psi - [V(x) + iW(x)]\psi + |\psi|^4\psi = 0. \tag{20}$$

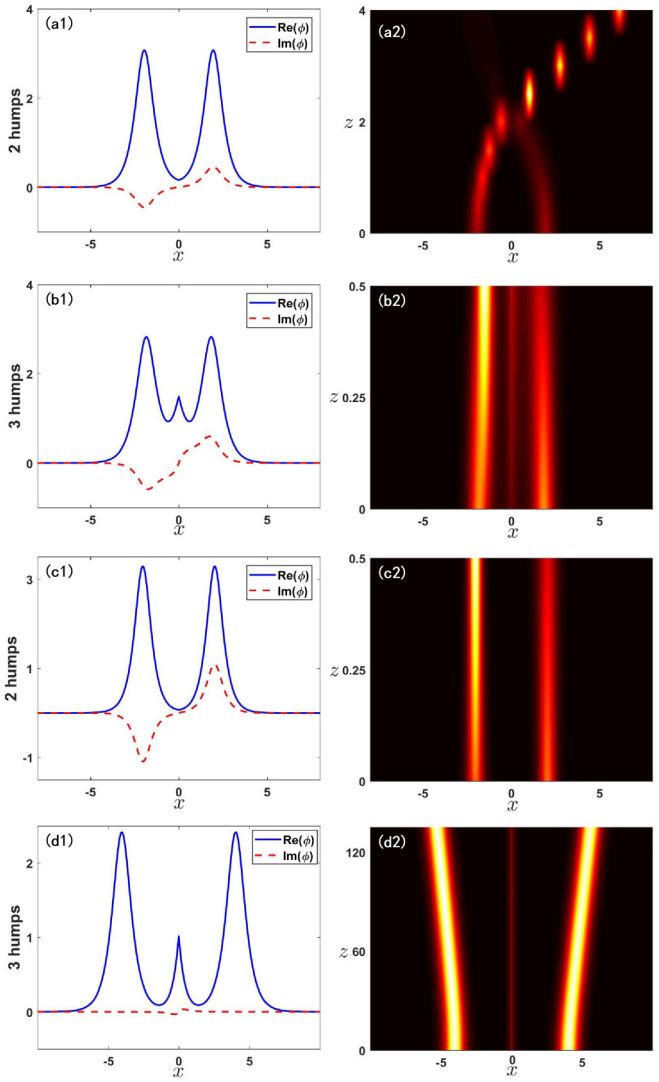

FIG. 10. Numerical high-order solitons and their wave propagations. (a1),(a2) Two-hump soliton of Eq. (6) with potential (2) at $W_0 = -0.4$, $\alpha = 0.5$, $\mu = 6$, $a = 6$, $b = 4$, $c = \sqrt{2}$; (b1),(b2) three-hump soliton of Eq. (6) with potential (2) at $W_0 = -2$, $\alpha = -1$, $\mu = 3$, $a = 6$, $b = 4$, $c = \sqrt{2}$; (c1),(c2) two-hump soliton of Eq. (6) with potential (4) at $W_0 = -0.4$, $\alpha = 0.5$, $\mu = 6$, $a = 4$, $b = 4$, $c = \sqrt{2}$; (d1),(d2) three-hump soliton of Eq. (6) with potential (4) at $W_0 = -2$, $\alpha = -2$, $\mu = 3$, $a = 6$, $b = 8$, $c = 2$.

We study the $\mathcal{PT}$-phase broken and unbroken curves by studying Eq. (5) with the potential (17) for $\beta = 1/\sigma = 2,\ 1/2$ [see Figs. 11(a1) and 11(b1)]. Meanwhile, we can conclude that the collisions of the first few energy levels can lead to the broken $\mathcal{PT}$ phase from Figs. 11(a2), 11(a3), 11(b2), and 11(b3). And to compare the effect of the nonlinear term and the $\mathcal{PT}$ phase on the soliton stability, we choose the same potential parameters as Figs. 4 and 5 when $\sigma = 2$ and $\sigma = 1/2$.

Case 1. $\sigma = 2$. For this case, we consider the quintic NLS equation (20). As $\alpha < 0$, we can find the stable wave propagations in Figs. 12(a1), 12(a2), 12(a5), and 12(a6) for the different parameters. However, in the $\mathcal{PT}$ unbroken region, we find an unstable dynamical behavior [see Figs. 12(a3) and 12(a4)], which is mainly due to the effect of the quintic nonlinear term $|\psi|^4\psi$ on the $\mathcal{PT}$ phase. For $\alpha > 0$, the double-hump solitons can stably propagate for a long time [see Figs. 12(b1)–12(b6)].

Case 2. $\sigma = 1/2$. For this case, we consider the quadratic NLS equation (19). As $\alpha < 0$, we obtain the stable peakon propagation at $\alpha = -1$, $W_0 = 1$ and $\alpha = -2$, $W_0 = 2.48$ [see Figs. 13(a1), 13(a2), 13(a5), 13(a6)]. Whereas $\alpha = -1$, $W_0 = 2.48$, Figs. 13(a3) and 13(a4) display the unstable dynamical behavior, which is mainly due to the nonlinear term $|\psi|\psi$. When $\alpha > 0$, we also consider the same parameters as in Fig. 5. The results are shown in Figs. 13(b1)–13(b6).

Compared with the numerical simulations in Figs. 4 and 5, it can be concluded that the stable solitons are modulated by both the $\mathcal{PT}$-symmetric potentials and the nonlinear terms, which balance each other to generate the solitons in the nonlinear dissipative system.

V. THE SOLITON INTERACTIONS

Here we examine the interactions of the solitary waves with the stable peakon solutions and the double-hump solutions. For $\alpha < 0$, we consider the following initial condition consisting of two peakon solutions:

$$\psi(x,0) = \phi(x) + \frac{W_0}{3}\mathrm{sech}(x-30)e^{\alpha|x-30|-6ix}, \tag{21}$$

where $\alpha = -0.02$, $W_0 = 0.5$, and the peakon solution $\phi(x)$ is given by Eq. (9). Figure 14(a1) indicates that there exists a semi-elastic interaction between the exact solution and the exotic isolated solitary wave, where the exact solution maintains its shape before and after the collision, while the intensity of the exotic isolated wave decays continuously, and there exists a very small reflected wave. In order to explore the more intriguing nature of a peakon soliton, we set the outside Gaussian solitary wave as $\frac{W_0}{3}e^{-0.01(x-50)^2-9ix}$, and $\alpha = -2$, $W_0 = 1$; that is, the initial condition is chosen as

$$\psi(x,0) = \phi(x) + \frac{W_0}{3}e^{-0.01(x-50)^2-9ix}. \tag{22}$$

Surprisingly, a new phenomenon arises in collisions, namely, there is not only the transmitted wave, but also the presence of a reflected wave after the interaction of an external incident wave and the exact peakon solution [see Fig. 14(a2)]. Figure 14(a3) shows the changes of densities before and after their collision. From this, we can see that the density of the exact peakon solution is not changed before and after the collision, but the exotic isolated Gaussian waves are separated into two branches after the collision. Moreover, the density of the transmitted (reflected) wave is slightly larger (smaller) than the initial density, which indicates that the energy of the solitons is transferred during the collision.

For the case of $\alpha > 0$, we choose the potential parameter $\alpha = 0.1$, $W_0 = 0.1$, and the outside solitary wave is added to the initial condition, which means the initial condition is chosen as follows:

$$\psi(x,0) = \phi(x) + \frac{W_0}{3}\mathrm{sech}(x-30)e^{\alpha|x-30|-10.5ix}. \tag{23}$$

Intriguingly, the collision of the stable double-hump solution with the solitary shows a "semi-elastic" phenomenon [see Fig. 14(b1)]. The double-hump solution remains invariant unless there is interaction of the two nonlinear waves, while

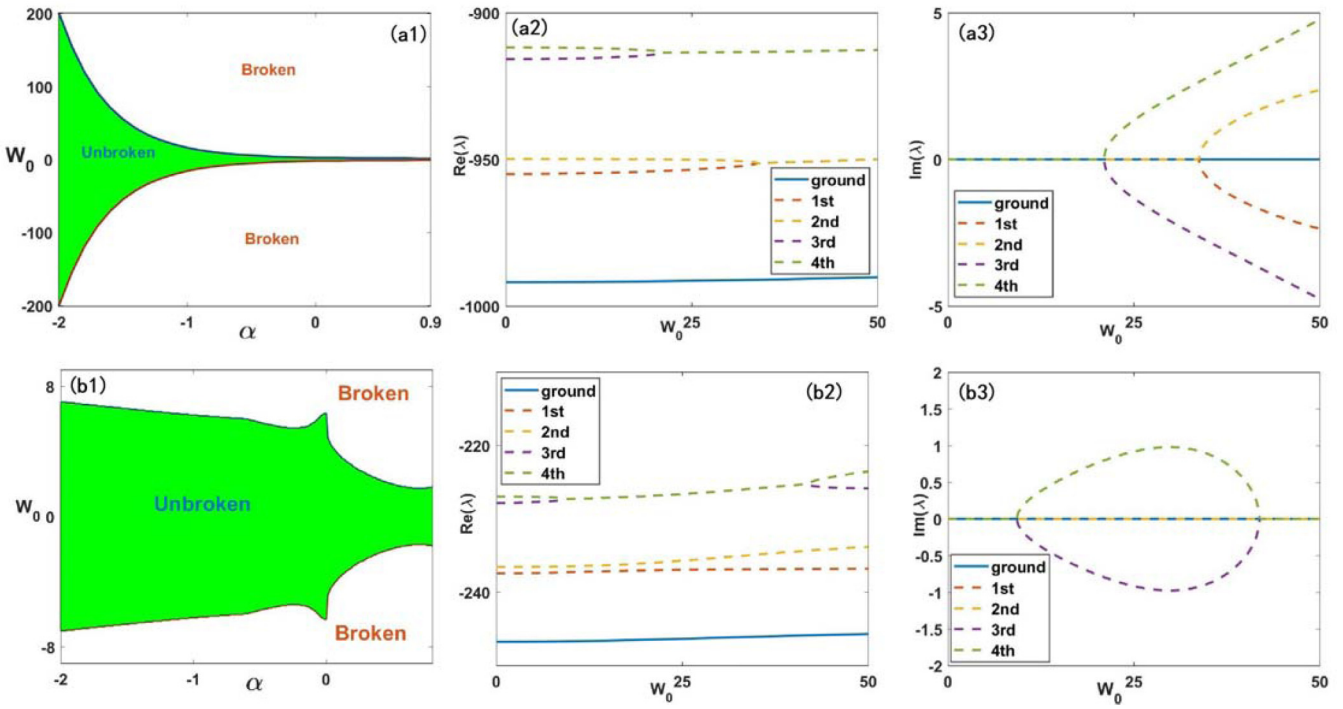

FIG. 11. The $\mathcal{PT}$-phase unbroken and broken curves of Eq. (5) with the potential (17) at (a1) $\sigma = 2$ and (b1) $\sigma = \frac{1}{2}$. Real and imaginary parts of the first five eigenvalues λ as a function of W_0 at (a2),(a3) $\alpha = -1,\ \sigma = 2$ and (b2),(b3) $\alpha = -1,\ \sigma = \frac{1}{2}$.

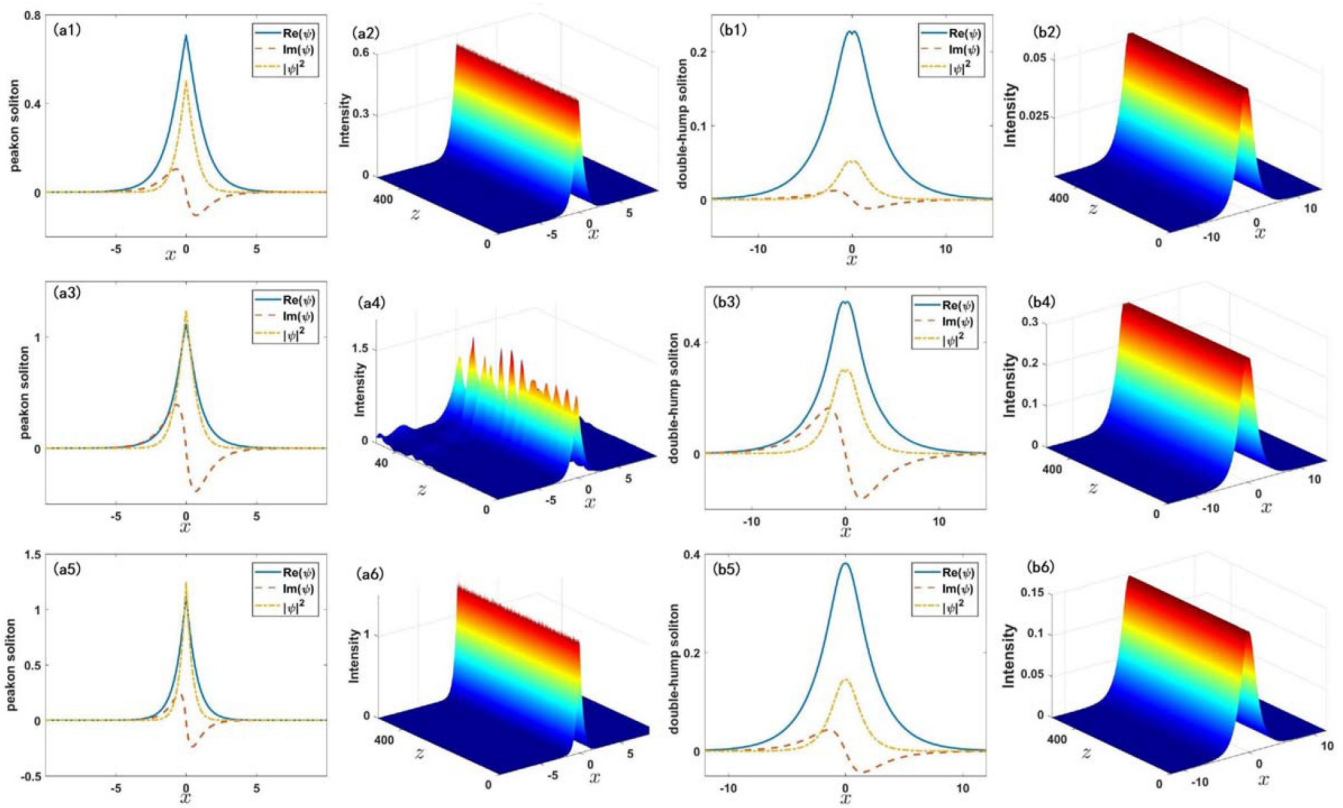

FIG. 12. The wave propagations with a 2% noise for solution (18) at $\sigma = 2$. (a1),(a2) $\alpha = -1, W_0 = 1$; (a3),(a4) $\alpha = -1, W_0 = 2.48$; (a5),(a6) $\alpha = -2, W_0 = 2.48$; (b1),(b2) $\alpha = 0.25, W_0 = 0.1$; (b3),(b4) $\alpha = 0.25, W_0 = 0.58$; (b5),(b6) $\alpha = 0.04, W_0 = 0.29$.

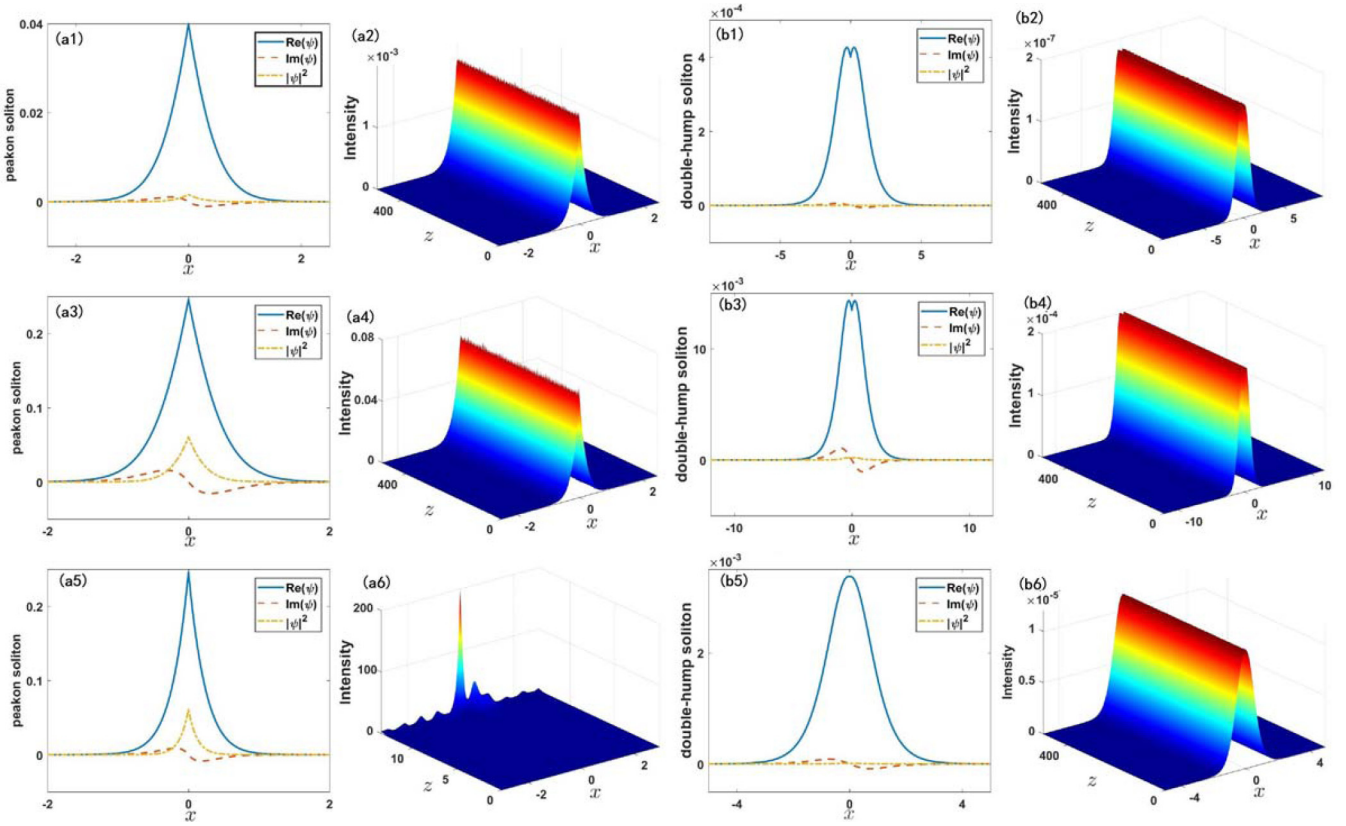

FIG. 13. The wave propagations with a 2% noise for solution (18) at $\sigma = \frac{1}{2}$. (a1),(a2) $\alpha = -1, W_0 = 1$; (a3),(a4) $\alpha = -1, W_0 = 2.48$; (a5),(a6) $\alpha = -2, W_0 = 2.48$; (b1),(b2) $\alpha = 0.25, W_0 = 0.1$; (b3),(b4) $\alpha = 0.25, W_0 = 0.58$; (b5),(b6) $\alpha = 0.04, W_0 = 0.29$.

the outside solitary wave decays slowly. At the same time, we can observe a very weak reflection phenomenon. Meanwhile, we change the outside wave to the Gaussian wave, $\frac{W_0}{3}e^{-0.05(x-20)^2-5.5ix}$, where $\alpha = 0.2, W_0 = 0.2$, which is the initial condition taken as

$$\psi(x,0) = \phi(x) + \frac{W_0}{3}e^{-0.05(x-20)^2-5.5ix}. \tag{24}$$

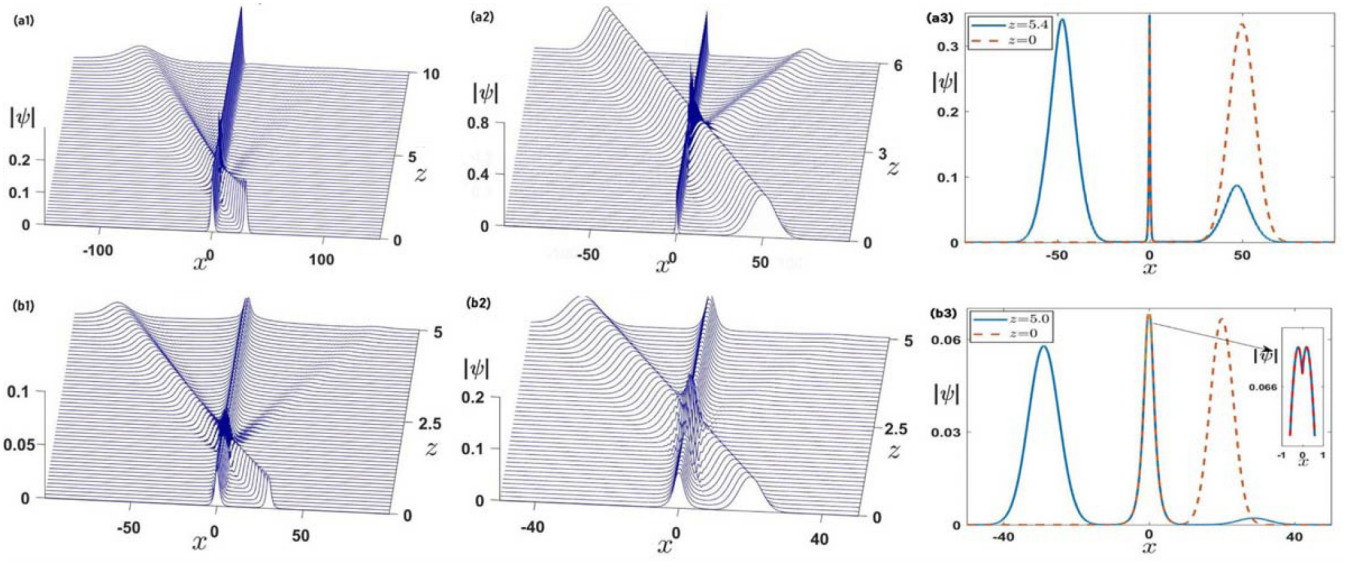

FIG. 14. Soliton interactions. (a1) $\alpha = -0.02$, $W_0 = 0.5$, outside peakon wave: $\frac{W_0}{3}\mathrm{sech}(x-30)e^{(\alpha|x-30|-6ix)}$; (a2) $\alpha = -2, W_0 = 1$, outside Gaussian solitary wave: $\frac{W_0}{3}e^{-0.01(x-50)^2-9ix}$; (a3) the collision profiles at differential values of z in (a2); (b1) $\alpha = 0.1, W_0 = 0.1$, outside double-hump soliton: $\frac{W_0}{3}\mathrm{sech}(x-30)e^{(\alpha|x-30|-10.5ix)}$; (b2) $\alpha = 0.2, W_0 = 0.2$, outside Gaussian solitary wave: $\frac{W_0}{3}e^{-0.05(x-20)^2-5.5ix}$; (b3) the collision profiles at differential values of z in (b2).

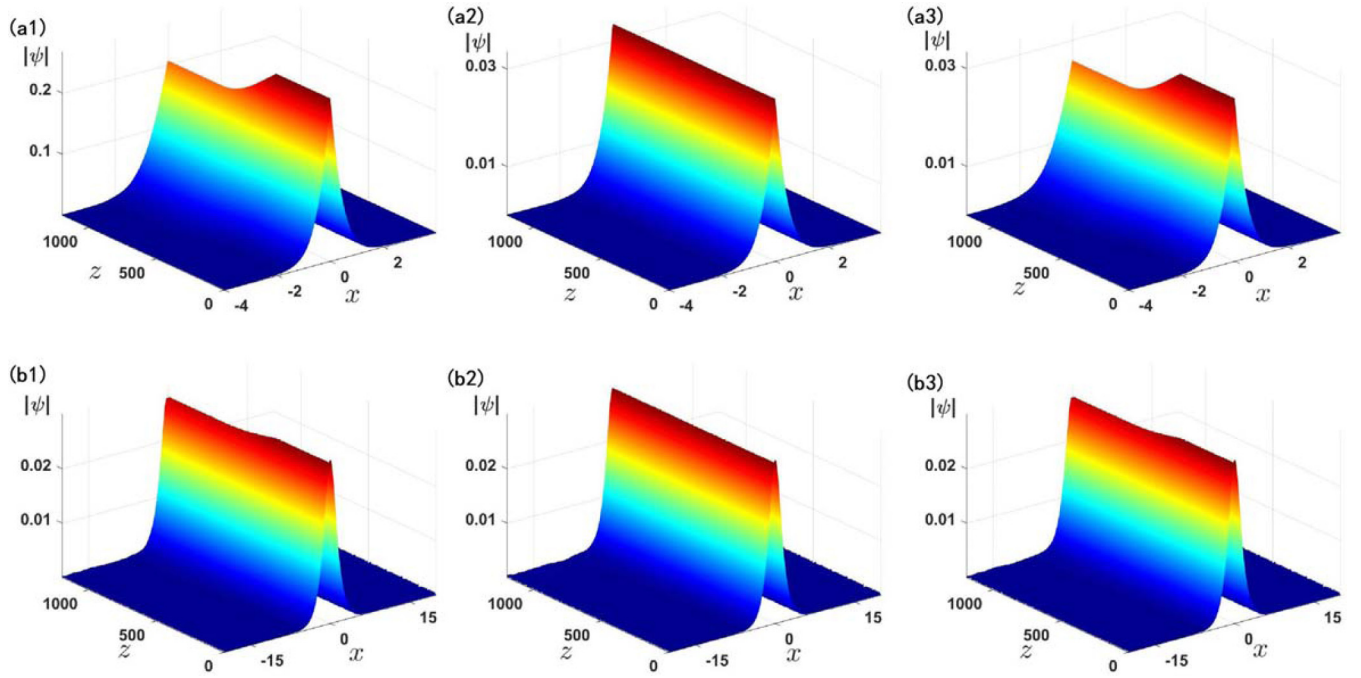

FIG. 15. Excitations of peakon solutions: (a1) $\alpha_i = -2$, $\alpha_e = -1$, $W_0 = 0.8$; (a2) $\alpha = -2$, $W_{0i} = 0.1$, $W_{0e} = 0.8$; (a3) $\alpha_i = -2$, $\alpha_e = -1$, $W_{0i} = 0.1$, $W_{0e} = 0.8$; (b1) $\alpha_0 = 0.05$, $\alpha_1 = 0.1$, $W_0 = 0.09$; (b2) $\alpha = 0.05$, $W_{01} = 0.09$, $W_{02} = 0.2$; (b3) $\alpha_0 = 0.05$, $\alpha_1 = 0.1$, $W_{01} = 0.09$, $W_{02} = 0.2$.

In a collision with an ordinary soliton (differential), as Fig. 14(b2) indicates, the exact solution forms a weak elastic collision with the exotic wave, which means the shape and intensity of the double-hump soliton with one gallery remain the same, and there exists a slight change in the external isolated wave. In order to observe the soliton behavior before and after the collision more clearly, the exotic Gaussian wave is shown in Fig. 14(b3) with a broadened center and a weak reflection after the collision, while the enlarged figure in Fig. 14(b3) illustrates the elastic behavior of the exact solution during the collision. The phenomena shown here are different from the case of $\alpha < 0$, which suggests that α can modulate the nature and shape of solitons.

VI. THE ADIABATIC EXCITATIONS OF SOLITONS

In this section, we change the parameters in the $\mathcal{PT}$-symmetric δ-Scarf-II potential as the functions of the propagation distance z, i.e., we apply an adiabatic switch to the δ-Scarf-II potential: $\alpha \to \alpha(z)$, $W_0 \to W_0(z)$. At this point, the propagation of the nonlinear modes is controlled by the equation

$$i\partial_z\psi + \partial_x^2\psi - [V(x,z) + iW(x,z)]\psi + |\psi|^2\psi = 0, \quad (25)$$

where $V(x,z)$ and $W(x,z)$ are determined by Eq. (2) with $V_0 \to V_0(z)$, $\alpha \to \alpha(z)$, $W_0 \to W_0(z)$, and $V_0(z)$, $\alpha(z)$, and $W_0(z)$ taken as

$$\varrho(z) = \begin{cases} \varrho_i, & 0 \leqslant z \leqslant 400 \\ \varrho_i + (\varrho_e - \varrho_i)\sin\left[\frac{(z-400)\pi}{800}\right], & 400 < z \leqslant 800 \\ \varrho_e, & 800 < z, \end{cases} \quad (26)$$

where ϱ_i and ϱ_e represent the parameters of the initial and termination states, respectively. It is easily verified that when $V_0(z) = 2\alpha(z)$ and an adiabatic switch (26) is applied to the potential, the nonlinear mode (9) satisfies Eq. (6), except for the initial state $0 \leqslant z \leqslant 400$ and the excited state $z > 800$. Since the positive or negative sign of α affects the nature of the excited final solution, we discuss two cases, where $\alpha < 0$ and $0 < \alpha < 1$.

A. Excitation of peakon solutions

For the considered Eq. (25) with $\alpha(z)$ or $W_0(z)$ given by Eq. (26), we consider the excitations of the stationary solution (9). First, we take $\psi(x,0) = \phi(x)$, with $\phi(x)$ given by Eq. (9) as the initial condition, and consider the case that $\alpha(z)$ is given by Eq. (26), while $W_0(z)$ is fixed as the constant W_0. As a result, we find that the initial nonlinear mode for $(\alpha_i, W_0) = (-2, 0.8)$ can be excited to another stable nonlinear mode for $(\alpha_e, W_0) = (-1, 0.8)$ [see Fig. 15(a1)]. Under this initial condition, it excites an initially stable peakon solution with a higher density to another stable peakon solution with a lower density. And due to the adiabatic condition (26), there exists a transition process between two stable propagations. Here, both the front and back modes correspond to the linear $\mathcal{PT}$-phase unbroken case. Similarly, if we fix $\alpha(z) \equiv \alpha$ and let $W_0(z)$ be given by Eq. (26), we can implement a similar excitation of stable exact nonlinear modes, as shown in Fig. 15(a2). In contrast to the first case, the density of the nonlinear mode remains almost unchanged during the excitation process. It is worth noting that W_0 can modulate the density, but the density still remains unchanged. This is mainly due to the fact that the density of the nonlinear mode hardly changes during the stable

excitation propagation. Finally, we apply an adiabatic switch to both parameters simultaneously; that is, the two functions $\alpha(z)$ and $W_0(z)$ are given by Eq. (26) [see Fig. 15(a3)], which can be considered as a simple superposition of the first two one-parameter excitations. That is why Fig. 15(c) looks very similar to Fig. 15(a1).

B. Excitation of double-hump soliton

As $0 < \alpha < 1$, Eq. (1) admits the double-hump solution with one sharp valley, similarly to the previous section for $\alpha < 0$. The specific results are shown in Figs. 15(b1)–15(b3). When we apply an adiabatic switch (26) to the parameter α, it initiates three stable propagation processes [see Fig. 15(b1)], which is related to the excitation condition (26). We also take $W_0(z)$ as the function of propagation distance given by Eq. (26), and the density remains almost unchanged [see Fig. 15(b2)]. Finally, when we apply the adiabatic switch to both parameters $\alpha(z)$, $W_0(z)$, the result [see Fig. 15(b3)] is similar to the case of the changed parameter $\alpha(z)$.

VII. CONCLUSIONS AND DISCUSSIONS

To summarize, we have introduced the $\mathcal{PT}$-symmetric Dirac δ-Scarf-II potential into the NLS equation and studied the real spectral region of the linear spectral problem, and discovered the stable peakon solutions and double-hump solitons in the self-focusing Kerr nonlinear media. At the same time, we find the stable wave propagations of peakons and double-hump solitons in the interplay between the power-law nonlinearity and $\mathcal{PT}$-symmetric potentials. Moreover, the existence of stable soliton excitation is also confirmed by applying an adiabatic switch, which indicates that the peakon solution and double-hump soliton are highly resistant to interference.

Furthermore, we have to mention that one can study the peakon solitons and double-hump solitons in the higher-dimensional case. Moreover, this kind of $\mathcal{PT}$-symmetric δ-Scarf-II potential can also be generalized to other nonlinear wave models, such as the derivative NLS equation, third-order NLS equation, etc.

ACKNOWLEDGMENTS

We would like to thank the referees for their valuable suggestions that have substantially improved our manuscript. The work of Z.Y. was supported by the NSFC under Grants No. 11925108 and No. 11731014. The work of Y.C. was supported by the NSFC under Grants No. 12001246 and No. 11947087, the NSF of Jiangsu Province of China (Grant No. BK20190991), and the NSF of Jiangsu Higher Education Institutions of China (Grant No. 19KJB110011). The work of S.-F.T. was supported by the NSFC under Grant No. 11975306, the NSF of Jiangsu Province of China (Grant No. BK20181351), and the Six Talent Peaks Project in Jiangsu Province (Grant No. JY-059).

[1] D. J. Griffiths and D. F. Schroeter, *Introduction to Quantum Mechanics* (Cambridge University Press, New York, 2018).

[2] C. M. Bender and S. Boettcher, Real Spectra in Non-Hermitian Hamiltonians having PT Symmetry, Phys. Rev. Lett. **80**, 5243 (1998).

[3] Z. Ahmed, Real and complex discrete eigenvalues in an exactly solvable one- dimensional complex PT-invariant potential, Phys. Lett. A **282**, 343 (2001).

[4] P. Dorey, C. Dunning, and R. Tateo, Spectral equivalences, Bethe ansatz equations, and reality properties in PT-symmetric quantum mechanics, J. Phys. A **34**, 5679 (2001).

[5] C. M. Bender, Making sense of non-Hermitian Hamiltonians, Rep. Prog. Phys. **70**, 947 (2007).

[6] C. M. Bender, Rigorous backbone of PT-symmetric quantum mechanics, J. Phys. A **49**, 401002 (2016).

[7] S. Longhi, Bloch Oscillations in Complex Crystals with PT Symmetry, Phys. Rev. Lett. **103**, 123601 (2009).

[8] B. Midya, B. Roy, and R. Roychoudhury, A note on the PT invariant periodic potential $V(x) = 4\cos^2 x + 4iV_0 \sin 2x$, Phys. Lett. A **374**, 2605 (2010).

[9] A. Guo, G. Salamo, D. Duchesne, R. Morandotti, M. Volatier-Ravat, V. Aimez, G. Siviloglou, and D. Christodoulides, Observation of PT-Symmetry Breaking in Complex Optical Potentials, Phys. Rev. Lett. **103**, 093902 (2009).

[10] C. E. Rüter, K. G. Makris, R. El-Ganainy, D. N. Christodoulides, M. Segev, and D. Kip, Observation of parity-time symmetry in optics, Nat. Phys. **6**, 192 (2010).

[11] A. Regensburger, C. Bersch, M.-A. Miri, G. Onishchukov, D. N. Christodoulides, and U. Peschel, Parity-time synthetic photonic lattices, Nature (London) **488**, 167 (2012).

[12] B. Peng, S. K. Ödemir, F. Lei, F. Monifi, M. Gianfreda, G. L. Long, S. Fan, F. Nori, C. M. Bender, and L. Yang, Parity-time-symmetric whispering-gallery microcavities, Nat. Phys. **10**, 394 (2014).

[13] H. Hodaei, A. U. Hassan, S. Wittek, H. Garcia-Gracia, R. ElGanainy, D. N. Christodoulides and M. Khajavikhan, Enhanced sensitivity at higher-order exceptional points, Nature (London) **548**, 187 (2017).

[14] B. Liu, H.-F. Zhang, R.-X. Zhong, X.-L. Zhang, X.-Z. Qin, C. Huang, Y.-Y. Li, and B. A. Malomed, Symmetry breaking of quantum droplets in a dual-core trap, Phys. Rev. A **99**, 053602 (2019).

[15] Z. Musslimani, K. G. Makris, R. El-Ganainy, and D. N. Christodoulides, Optical Solitons in PT Periodic Potentials, Phys. Rev. Lett. **100**, 030402 (2008).

[16] F. K. Abdullaev, V. V. Konotop, M. Salerno, and A. V. Yulin, Dissipative periodic waves, solitons, and breathers of the nonlinear Schrödinger equation with complex potentials, Phys. Rev. E **82**, 056606 (2010).

[17] F. K. Abdullaev, Y. V. Kartashov, V. V. Konotop, and D. A. Zezyulin, Solitons in PT-symmetric nonlinear lattices, Phys. Rev. A **83**, 041805(R) (2011).

[18] Z. Shi, X. Jiang, X. Zhu, and H. Li, Bright spatial solitons in defocusing Kerr media with PT-symmetric potentials, Phys. Rev. A **84**, 053855 (2011).

[19] N. Moiseyev, Crossing rule for a PT-symmetric two-level time-periodic system, Phys. Rev. A **83**, 052125 (2011).

[20] D. A. Zezyulin and V. V. Konotop, Nonlinear Modes in Finite-Dimensional Pt-Symmetric Systems, Phys. Rev. Lett. **108**, 213906 (2012).

[21] S. Nixon, L. Ge, and J. Yang, Stability analysis for solitons in PT-symmetric optical lattices, Phys. Rev. A **85**, 023822 (2012).

[22] S. Nixon, Y. Zhu, and J. Yang, Nonlinear dynamics of wave packets in parity-time-symmetric optical lattices near the phase transition point, Opt. Lett. **37**, 4874 (2012).

[23] V. Achilleos, P. Kevrekidis, D. Frantzeskakis, and R. Carretero-Gonzalez, Dark solitons and vortices in PT-symmetric nonlinear media: From spontaneous symmetry breaking to nonlinear PT phase transitions, Phys. Rev. A **86**, 013808 (2012).

[24] D. A. Zezyulin and V. V. Konotop, Nonlinear modes in the harmonic PT-symmetric potential, Phys. Rev. A **85**, 043840 (2012).

[25] Z. Yan, Complex PT-symmetric nonlinear Schrödinger equation and Burgers equation, Philos. Trans. R. Soc. A **371**, 20120059 (2013).

[26] Y. V. Bludov, V. V. Konotop, and B. A. Malomed, Stable dark solitons in PT-symmetric dual-core waveguides, Phys. Rev. A **87**, 013816 (2013).

[27] Y. Lumer, Y. Plotnik, M. C. Rechtsman, and M. Segev, Nonlinearly Induced PT Transition in Photonic Systems, Phys. Rev. Lett. **111**, 263901 (2013).

[28] Z. Yan, Z. Wen, and C. Hang, Spatial solitons and stability in self-focusing and defocusing Kerr nonlinear media with generalized parity-time-symmetric Scarf-II potentials, Phys. Rev. E **92**, 022913 (2015).

[29] Z. Yan, Z. Wen and V. V. Konotop, Solitons in a nonlinear Schrödinger equation with PT-symmetric potentials and inhomogeneous nonlinearity: Stability and excitation of nonlinear modes, Phys. Rev. A **92**, 023821 (2015).

[30] P. G. Kevrekidis, J. Cuevas-Maraver, A. Saxena *et al.*, Interplay between parity-time symmetry, supersymmetry, and nonlinearity: An analytically tractable case example, Phys. Rev. E **92**, 042901 (2015).

[31] Y. Chen, Z. Yan, and D. Mihalache, Soliton formation and stability under the interplay between parity-time-symmetric generalized Scarf-II potentials and Kerr nonlinearity, Phys. Rev. E **102**, 012216 (2020).

[32] Y. Chen and Z. Yan, Stable parity-time-symmetric nonlinear modes and excitations in a derivative nonlinear Schrödinger equation, Phys. Rev. E **95**, 012205 (2017).

[33] Y. Chen and Z. Yan, Solitonic dynamics and excitations of the nonlinear Schrödinger equation with third-order dispersion in non-Hermitian PT-symmetric potentials, Sci. Rep. **6**, 23478 (2016).

[34] Y. Chen, Z. Yan, D. Mihalache, and B. A. Malomed, Families of stable solitons and excitations in the PT-symmetric nonlinear Schrödinger equations with position-dependent effective masses, Sci. Rep. **7**, 1257 (2017).

[35] C.-Q. Dai, X.-G. Wang, and G.-Q. Zhou, Stable light-bullet solutions in the harmonic and parity-time-symmetric potentials, Phys. Rev. A **89**, 013834 (2014).

[36] M. Znojil, Quantum phase transitions in nonhermitian harmonic oscillator, Sci. Rep. **10**, 1 (2020).

[37] S. Hu, X. Ma, D. Lu, Z. Yang, Y. Zheng, and W. Hu, Solitons supported by complex PT-symmetric Gaussian potentials, Phys. Rev. A **84**, 043818 (2011).

[38] J. Yang, Symmetry breaking of solitons in one-dimensional parity-time symmetric optical potentials, Opt. Lett. **39**, 5547 (2014).

[39] W.-X. Xu, S.-J. Su, B. Xu, Y.-W. Guo, S.-L. Xu, Y. Zhao and Y.-H. Hu, Two dimensional spacial soliton in atomic gases with PT-symmetry potential, Opt. Express **28**, 35297 (2020).

[40] C. P. Jisha, L. Devassy, A. Alberucci, and V. Kuriakose, Influence of the imaginary component of the photonic potential on the properties of solitons in PT-symmetric systems, Phys. Rev. A **90**, 043855 (2014).

[41] A. Das, N. Ghosh and D. Nath, Stable modes of derivative nonlinear Schrödinger equation with super-Gaussian and parabolic potential, Phys. Lett. A **384**, 126681 (2020).

[42] G.-H. Sun and S.-H. Dong, Quantum information entropies of the eigenstates for a symmetrically trigonometric Rosen-Morse potential, Phys. Scr. **87**, 045003 (2013).

[43] B. Midya and R. Roychoudhury, Nonlinear localized modes in PT-symmetric Rosen-Morse potential wells, Phys. Rev. A **87**, 045803 (2013).

[44] Y. He and D. Mihalache, Lattice solitons in optical media described by the complex Ginzburg-Landau model with PT-symmetric periodic potentials, Phys. Rev. A **87**, 013812 (2013).

[45] Z. Zhang, Y. Zhang, J. Sheng, L. Yang, M. A. Miri, D. N. Christodoulides and M. Xiao, Observation of parity-time symmetry in optically induced atomic lattices, Phys. Lett. A **117**, 123601 (2016).

[46] R. Fortanier, D. Dast, D. Haag, H. Cartarius, J. Main, G. Wunner, and R. Guöhrlein, Dipolar Bose-Einstein condensates in a PT-symmetric double-well potential, Phys. Rev. A **89**, 063608 (2014).

[47] P. Li and D. Mihalache, Symmetry breaking of solitons in PT-symmetric potentials with competing cubic-quintic nonlinearity, Proc. Rom. Acad. A **19**, 61 (2018).

[48] R. J. Lombard, R. Mezhoud, and R. Yekken, Complex potentials with real eigenvalues and the inverse problem, Rom. J. Phys. **63**, 101 (2018).

[49] N. Moiseyev, *Non-Hermitian Quantum Mechanics* (Cambridge University Press, Cambridge, 2011).

[50] V. V. Konotop, J. Yang, and D. A. Zezyulin, Nonlinear waves in PT-symmetric systems, Rev. Mod. Phys. **88**, 035002 (2016).

[51] S. V. Suchkov, A. A. Sukhorukov, J. Huang, S. V. Dmitriev, C. Lee, and Y. S. Kivshar, Nonlinear switching and solitons in PT-symmetric photonic systems, Laser Photon. Rev. **10**, 177 (2016).

[52] D. Mihalache, Multidimensional localized structures in optical and matter-wave media: a topical survey of recent literature, Rom. Rep. Phys. **69**, 403 (2017).

[53] D. Christodoulides and J. Yang, *Parity-time Symmetry and Its Applications* (Springer, Berlin, 2018).

[54] R. El-Ganainy, K. G. Makris, M. Khajavikhan, Z. H. Musslimani, S. Rotter, and D. N. Christodoulides, Non-Hermitian physics and PT symmetry, Nat. Phys. **14**, 11 (2018).

[55] Y. Zhang, Z. Chen, B. Wu, T. Busch, and V. V. Konotop, Asymmetric Loop Spectra and Unbroken Phase Protection due to Nonlinearities in Pt-Symmetric Periodic Potentials, Phys. Rev. Lett. **127**, 034101 (2021).

[56] Y. S. Kivshar and G. Agrawal, *Optical Solitons: From Fibers to Photonic Crystals* (Academic Press, San Diego, 2003).

[57] G. Agrawal, *Applications of Nonlinear Fiber Optics* (Elsevier, Amsterdam, 2001).

[58] H. Cartarius and G. Wunner, Model of a PT-symmetric Bose-Einstein condensate in a δ-function double-well potential, Phys. Rev. A **86**, 013612 (2012).

[59] T. Mayteevarunyoo, B. A. Malomed, and A. Reoksabutr, Solvable model for solitons pinned to a parity-time-symmetric dipoles, Phys. Rev. E **88**, 022919 (2013).

[60] I. Barashenkov and D. Zezyulin, Localised nonlinear modes in the PT-symmetric double-delta well Gross-Pitaevskii equation, in *Non-Hermitian Hamiltonians in Quantum Physics*, edited by F. Bagarello, R. Passante, and C. Trapani (Springer, New York, 2016), pp. 123.

[61] I. Barashenkov, D. Zezyulin, and V. Konotop, Jamming anomaly in PT-symmetric systems, New J. Phys. **18**, 075015 (2016).

[62] L. Wang, B. A. Malomed, and Z. Yan, Attraction centers and parity-time-symmetric delta-functional dipoles in critical and supercritical self-focusing media, Phys. Rev. E **99**, 052206 (2019).

[63] Y. Chen, Z. Yan and D. Mihalache, Stable flat-top solitons and peakons in the PT-symmetric delta-signum potentials and nonlinear media, Chaos **29**, 083108 (2019).

[64] G. Lévai and M. Znojil, The interplay of supersymmetry and PT symmetry in quantum mechanics: a case study for the Scarf II potential, J. Phys. A. **35**, 8793 (2002).

[65] B. Bagchi, B and C. Quesne, An update on the-symmetric complexified Scarf II potential, spectral singularities and some remarks on the rationally extended supersymmetric partners, J. Phys. A. **43**, 305301 (2010).

[66] L. N. Trefethen, *Spectral Methods in Matlab* (SIAM, Philadelphia, 2000).

[67] J. Shen and T. Tang, *Spectral and High-order Methods with Applications* (Science Press, Beijing, 2006).

[68] J. Yang, *Nonlinear Waves in Integrable and Nonintegrable Systems* (SIAM, Philadelphia, 2010).

[69] S. Flügge, *Practical Quantum Mechanics* (Springer Science Business Media, New York, 2012).

[70] M. J. Ablowitz and Z. H. Musslimani, Spectral renormalization method for computing self-localized solutions to nonlinear systems, Opt. Lett. **30**, 2140 (2005).

[71] J. Yang and T. I. Lakoba, Universally-convergent squared-operator iteration methods for solitary waves in general nonlinear wave equations, Stud. Appl. Math. **118**, 153 (2007).

[72] D. Haag, D. Dast, A. Lohle, H. Cartarius, J. Main and G. Wunner, Nonlinear quantum dynamics in a $\mathcal{PT}$-symmetric double well, Phys. Rev. A **89**, 023601 (2014).